UNIVERSIDADE DE LISBOA
FACULDADE DE CIÊNCIAS
DEPARTAMENTO DE FÍSICA

Microfabrication of a cantilever probe

João Teodoro da Silva Freitas

Mestrado Integrado em Engenharia Física

Dissertação orientada por:
Dr. Mário Manuel Silveira Rodrigues
Dr. João Maria Melo Albuquerque Saraiva Mouro

2020

Acknowledgements

First, I would like to thank Professor Susana Freitas for the opportunity to develop this project at INESC-MN and to Professor Margarida Cruz for the kindness of giving me a project which satisfied my interests.

From INESC-MN, a big thanks to João Mouro for guiding me during this project, always answering my doubts and helping me during the project. To all the process engineers, for helping and teaching me about the cleanroom and its machines, especially to Eng. Virgínia Soares for the countless times she assisted me on the project. To Ana Silva and Jorge Pereira for the help and insights and everyone else who helped me with this project.

From AFM-RT, I want to thank my supervisor Professor Mário Rodrigues for teaching me about Atomic Force Microscopy and the physics related to it, and to Tiago Robalo for teaching and assisting me on operating the AFM.

To the friends that accompanied me during this five-year journey helping me during both my best and worst times. Especially to Gabriela, Sofia, Inês and Primos thank you so much. To the friends from before college that helped me get through these years with simple gestures, such as taking me out of my house for a fast coffee: João, Valéria, Adriana, Margarida and everyone from O Balde. A special thanks to Ricardo and Laura, for dealing with my tantrums with the thesis writing.

Last but not least, to the people who enabled all this to be possible, mom and dad. Thank you so much for everything, for giving me an education and for the endless support you gave me throughout these years, I love you so much.

Abstract

In this dissertation, microcantilevers are designed and fabricated. The cantilevers were dimensioned to be used in Atomic Force Microscopy in static and dynamic mode. Structures with different geometries were analysed, namely rectangular cantilevers, arrow-ended cantilevers, cantilevers with a hollow section and with different tips at the end.

This work aims to obtain a cantilever with both a hollow section and a tip allowing it to be used in AFM and as a nanoparticle dispenser. Various approaches and materials were tested during the fabrication to obtain the desired features. The tips were successfully fabricated and characterized independently of the cantilever. The hollow section was not fully characterised, but it was possible to observe that the channel was closed.

Silicon nitride cantilevers were successfully fabricated, however, due to the anomalous chip format, these could not be tested in a sample.

Keywords: Atomic Force Microscopy, Microfabrication, Cantilever, Microfluidics

Resumo

Nesta dissertação foram desenhados e fabricados *microcantilevers*. Os *cantilevers* foram dimensionados para serem utilizados em Microscopia de Força Atómica nos modos estático e dinâmico. Estes foram analisados assumindo diferentes geometrias nomeadamente *cantilevers* retangulares, *cantilevers* com uma extremidade triangular, *cantilevers* com uma seção oca e com diferentes pontas no final.

Este trabalho tem como objetivo obter um *cantilever* com uma seção oca e uma ponta permitindo que seja utilizado no AFM e como dispensador de nanopartículas. Várias abordagens e materiais foram testados durante a fabricação para obter as propriedades desejadas.

Inicialmente foi medida a taxa de erosão no plano (100) do silício para uma solução de KOH de 85 % (m/m), que resultou em $(0,44 \pm 0,01)$ µm/min e $(1,70 \pm 0,01)$ µm/min para uma temperatura de 60 ºC e 80 ºC respetivamente.

Inicialmente foi testado um procedimento para obter um *cantilever* de silício com e sem ponta. Foi possível obter um *cantilever* simples, fixado ao substrato, com uma espessura de 10 µm. Porém, a litografia para definir a ponta no topo deste *cantilever* não ficou bem definida, possivelmente devido ao facto de o laser não focar nos planos separados de 10 µm ou pelo fotoresiste não apresentar uma boa uniformidade ao longo da amostra, devido à espessura dos *cantilevers*. De modo a averiguar esta impossibilidade de definir a ponta no topo da estrutura foi testado um *cantilever* de silício com 1 µm de espessura. A etapa de litografia definiu com sucesso uma ponta no *cantilever*, no entanto, o contorno da estrutura tornou-se irregular ao longo processo de erosão por KOH para definir a ponta. Estes *cantilevers* de silício foram protegidos com uma camada de crómio e ouro, e titânio e ouro que não resistiram, para além de 1 hora, à erosão de KOH. Este procedimento foi efetuado numa amostra com um lado polido e outro não polido. O chip foi definido no lado não polido por ser de dimensões macroscópicas, onde o contorno não precisava ter alta resolução. No entanto, o Si_3N_4 que definiu a estrutura, após 2 horas de erosão com KOH, foi totalmente erodido deixando o chip desprotegido. Por esta razão, procedeu-se para a utilização de amostras com ambas as faces polidas para a fabricação de *cantilevers* de Si_3N_4.

O procedimento para obter os *cantilevers* de Si_3N_4 é muito semelhante ao de silício. Na etapa em que a amostra é erodida com KOH, o Si_3N_4 usado para proteger as estruturas

acabou por ser erodido após 2 horas. De modo a obter *cantilevers* suspensos procedeu-se a um método que não requeria tanto tempo de erosão com KOH. Estes foram obtidos com sucesso, porém, devido ao formato do chip estes não podem ser utilizados em microscopia de força atómica por não permitirem simultaneamente a interação com uma amostra e com o laser no topo do *cantilever*.

Independentemente do fabrico dos *cantilevers*, as pontas foram fabricadas e caracterizadas com sucesso junto com os seus parâmetros de fabricação. Duas pontas foram obtidas: uma cónica e outra piramidal. Estas pontas formam-se a partir da erosão anisotrópica do silício no quadrado de Si_3N_4 impresso, esta erosão foi medida e tem um valor de $etch_{dia} = (0,76 \pm 0,02)$ µm/min ao formar uma ponta cónica com um ângulo de $\alpha_{con} = (65 \pm 15)°$. Para a ponta piramidal foi medida uma taxa de erosão para o plano (111) do silício de $etch_{111} = (0,21 \pm 0,02)$ µm/min.

Relativamente aos canais ocos foi possível observar que os canais se encontravam selados após o passo de PECVD e que estes não colapsaram após 1 hora de erosão com KOH.

As propriedades físicas dos cantiléveres fabricados não foram medidas devido às dimensões do chip não corresponderem às do suporte de AFM. Estes foram excitados na plataforma da amostra do AFM, porém os atuadores piezoelétricos desta não tinham amplitude suficiente para os cantiléveres oscilarem.

Foram obtidos valores de frequência de ressonância para diferentes geometrias de *cantilevers* pelo método de elementos finitos, no entanto estes não puderam ser validados com resultados experimentais. Com esta caracterização, seria possível deduzir $\sqrt{E/\rho}$ para o Si_3N_4 depositado, para que futuros cantiléveres possam ser melhor dimensionados.

Palavras-chave: Microscopia de Força Atómica, Microfabricação, Cantiléver, Microfluídica

Contents

List of Figures

List of Tables

Acronyms

AFM	Atomic Force Microscopy
AM-AFM	Amplitude Modulation AFM
DPN	Dip-pen Nanolithography
FEM	Finite Element Method
FIB	Focused Ion Beam
FM-AFM	Frequency Modulation AFM
FPL	Fountain pen based lithography
FWHM	Full Width Half Maximum
HMDS	Hexamethyl disilizane
ICM	Intermittent Contact Mode
LPCVD	Low-Pressure Chemical Vapour Deposition
NADIS	Nano-Scale Dispensing
NCM	Non Contact Mode
PECVD	Plasma Enhanced Chemical Vapour Deposition
PMMA	Polydimethylsiloxane
PR	Photoresist
RIE	Reactive Ion Ecthing
SEM	Scanning Electron Microscopy
SPM	Scanning Probe Microscopy

STM Scanning Tunneling Microscopy

Symbols

Sign	Description	Unit
F	Force	N
k	Stiffness Constant	Nm^{-1}
Δz	Vertical Displacement	m
ω_0	Resonant Radial Frequency	rads^{-1}
$m*$	Effective mass	kg
α	Damping Coefficient	
z_d	Displacement of the cantilever holder	m
A_d	Oscillation Amplitude of the cantilever holder	m
Q	Quality factor	
A_0	Oscillation Amplitude of the cantilever	m
ϕ	Phase difference	rad
τ	Response time	s
M	Bending Moment	Nm
I	Moment of Inertia	kgm^2
E	Young Modulus	Pa
P	Point Load	N
L	Length of the cantilever	m
W	Width of the cantilever	m
T	Thickness of the cantilever	m
h_{tip}	Height of the tip	m
N_d	Nozzle diameter	m
k_{lat}	Lateral stiffness constant	Nm^{-1}
k_{tor}	Torsional stiffness	Nm^{-1}
G	Modulus of rigidity	Pa
v	Poisson ratio	
ρ_l	Mass per unit length	kgm^{-1}
t_c	Hollow thickness of the cantilever	m
w_c	Hollow width of the cantilever	m
Re	Reynold Number	
ρ	Density	kgm^{-3}

Sign	Description	Unit
v	Mean fluid velocity	m^{-1}
η	Dynamic viscosity	Pas
R	Channel radius	m
A_c	Channel cross-section area	m^2
P_c	Channel perimeter	m
Δp	Pressure drop	Pa
σ	Interfacial tension	Nm^{-1}
θ_c	Contact angle	rad
$etch_{100}$	Etch rate of the (100) silicon plane	ms^{-1}
$etch_{dia}$	Diagonal etch rate	ms^{-1}
$etch_{111}$	Etch rate of the (111) silicon plane	ms^{-1}
W_{lit}	Width printed in the lithography	m
α_{con}	Angle of the conical tip	rad

Chapter 1

Introduction

Nanotechnology is an area of research that has gained increasing interest due to its promising applications in our everyday lives and also for supporting the development of many other scientific fields. Atomic Force Microscopy is a technique that allows physical, chemical or biological interactions at the nanoscale using a cantilever with a sharp tip that interacts locally with a sample. Together with a piezoelectric set-up that moves the sample it is possible to have a precise and high resolution motion. When complementing this technique with microfluidics it gains the ability to dispense/aspirate liquids becoming a nanolithography tool which can manipulate matter allowing surface modification. The scope of this dissertation is to design and fabricate a microfluidic probe for ordered deposition of nanoparticles. The probe consists of a hollow Atomic Force Microscopy cantilever which will be mounted on a regular AFM optical beam detection configuration.

1.1 Objectives

The aim of this work consists in the fabrication of a hollow cantilever probe which could be used for atomic force microscopy imaging and for controlled deposition of nanoparticles in a substrate. The work starts from well established techniques and materials to fabricate cantilevers, which are then further improved to achieve the desired probe. From the simplest probe to the desired one, dimensioning, drawing and simulation are performed. The objectives are defined as follows:

- Fabrication of a cantilever;
- Fabrication of a cantilever with a tip;
- Fabrication of a cantilever with a hollow channel;
- Characterisation of the probe;

1.2 State of the Art

The interest in tools for deposition of small amounts of material on a nanoscale at specific positions is continuously increasing. Being able to control the spot size of the dispensed liquid brings both technologic and economic advantages. Fluidic Force Microscopy (FluidFM) technology joins the best features in Atomic Force Microscopy (AFM) and microfluidics. AFM is a technique that, besides being used as a microscope and for force spectroscopy, can also be used for manipulation of matter, since the tip interacts with the sample allowing changes of the sample properties and even displacement of matter. Further improvement of this technique can be achieved by using a microchanneled cantilever, enabling manipulation at the nanoscale and the dispensing and handling of small amounts of liquids and particles [1–6]. In order to achieve this, the AFM's cantilever needs to be modified to make the deposition of liquids possible. This type of approach gives origin to liquid deposition techniques such as, Dip-Pen Nanolithography (DPN) [7], Nano-Scale Dispensing (NADIS) [8], Fountain Pen Nanolithography (FPN) [9] and Scanning Ion Pipette (SIP) [10].

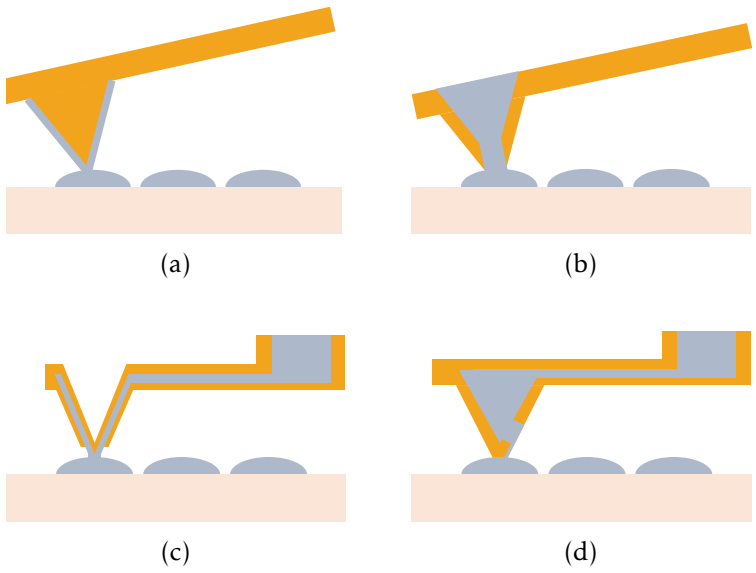

Figure 1.1: Representation of (a) a DPN, (b) a NADIS, (c) FPN and (d) SIP cantilever design (Adapted from [11]).

In DPN the cantilever tip is dipped in an "ink" and, as it touches a substrate, the molecular compounds in the tip are diffused to the substrate (Figure 1.1d). This technique allows patterning with resolutions of the order of nanometers. However, to print a wide pattern the tip needs to be dipped several times, which is time consuming and can originate alignment problems [12]. To overcome this limitation, the NADIS tool [8] was presented in 2003 (Figure 1.1b). The cantilever has a hollow pyramid with an aperture at the apex, allowing the dispensing of more liquid compared to DPN. In the NADIS device, liquid does not flow through the aperture by gravity alone. Instead, it is

Table 1.1: Characteristics of the different dispensing probes (Adapted from [12]).

		DPN	NADIS [2, 8]	FPN [9]	SIP [5, 6]
Material		Si	$Si/Si_3N_4/SiO_2$ Si_3N_4 Tip	Si_3N_4	SiO_2
Dim. [µm]	L	125	145-620	300-500	155
	W	30	110	20	6.4
	T	4	1-8	1.5	4.9
	h_{tip}	10-15	—	4	2.2
	w_c	—	—	5	3.7
	t_c	—	—	0.5	2.2
	N_d	—	0.1-1	—	0.3-2
AFM Mode		Contact	Contact	Contact	Contact Non-Contact

dispensed by bringing the sample surface in contact with the probe, having the liquid wet the surface in such a way that, when the probe is lifted, a small amount of liquid remains on the surface [13]. However, the resolution of this technique is reduced since the aperture is in the apex and, since the cantilever has no integrated microchannels, the liquid is loaded directly onto the cantilever. Such design proved to be a limitation, since substances like water would evaporate within a few seconds, and its use would then be restricted to liquids with low volatility, like glycerol. The evaporation problem can be overcome by connecting the hollow cantilever with a fluidic reservoir [13]. Devices with the hollow cantilever connected to a liquid reservoir were then reported a year later [14]. The FPN cantilever (Figure 1.1c) avoids realignment issues and evaporation problems by having its own fluidic reservoir. Contrarily to NADIS, this probe contains a sharp tip to ensure a high-resolution lithography. To have both these properties the tip presents a volcano-like shape [9]. The SIP probe presents the same advantages as the FPN, differing on the fabrication process. It results in a silicon oxide cantilever and the aperture can be placed either on the apex or close to it through focused ion milling [10]. These probes can also integrate an evaporation cell connected to the fluidic reservoir through a U-shaped channel passing through the cantilever tip, allowing the aspiration of liquids [4, 5, 15].

Table 1.1 outlines the characteristics of these probes, namely their material, their AFM modes and their typical dimensions, where L is the length, W the width, T the thickness of the cantilever, h_{tip} the tip height, N_d the nozzle diameter in the tip, w_c the width and t_c the thickness of the hollow channel.

Only silicon-based probes have been successfully tested, although on a different approach, SU-8 is commonly used for microfluidic applications and AFM cantilevers made of SU-8 have been already fabricated. The SU-8 hollow cantilevers that have been fabricated do not show any fluidic and AFM capability. There is also ongoing research on the fabricating of hollow SU-8/silicon, SU-8/PDMS (polydimethylsiloxane) and SU-8/PMMA (Poly(methyl methacrylate)) cantilevers [14].

Hollow cantilevers with integrated microfluidics channels can be fabricated in several ways depending on the choice of the material. Regardless, the fabrication can be divided into two steps: fabrication of the hollow tip cantilever and fabrication of the fluidic reservoir [5]. For silicon-based cantilevers there are two main processes: the "sacrificial layer" and the "thermal bonding" processes. The apertures in the cantilevers can either be fabricated through corner lithography [16, 17] or drilled by focused ion beam (FIB) [14].

The thermal bonding method results in a suspended and transparent SiO_2 microfluidic structure. Since the hollow AFM cantilever is made of SiO_2, the motion of the fluid can be visible with an optical microscope. In addition, SiO_2 is a good material due to its chemical, optical and electric/isolating properties [5, 10]. The second version of the NADIS [10] was produced by thermal bonding (Figure 1.2a). This method consists in the following steps [5, 10, 14]: (A) Etching of an inverted pyramid on a <100> silicon wafer; (B) Etching of the channel; (C) Deposition of Si_3N_4 at the tip (by corner lithography); (D) Etching of a second silicon wafer (for the reservoir); (E) Alignment and thermal oxide growth; and (F) The channel is released using KOH anisotropic etching.

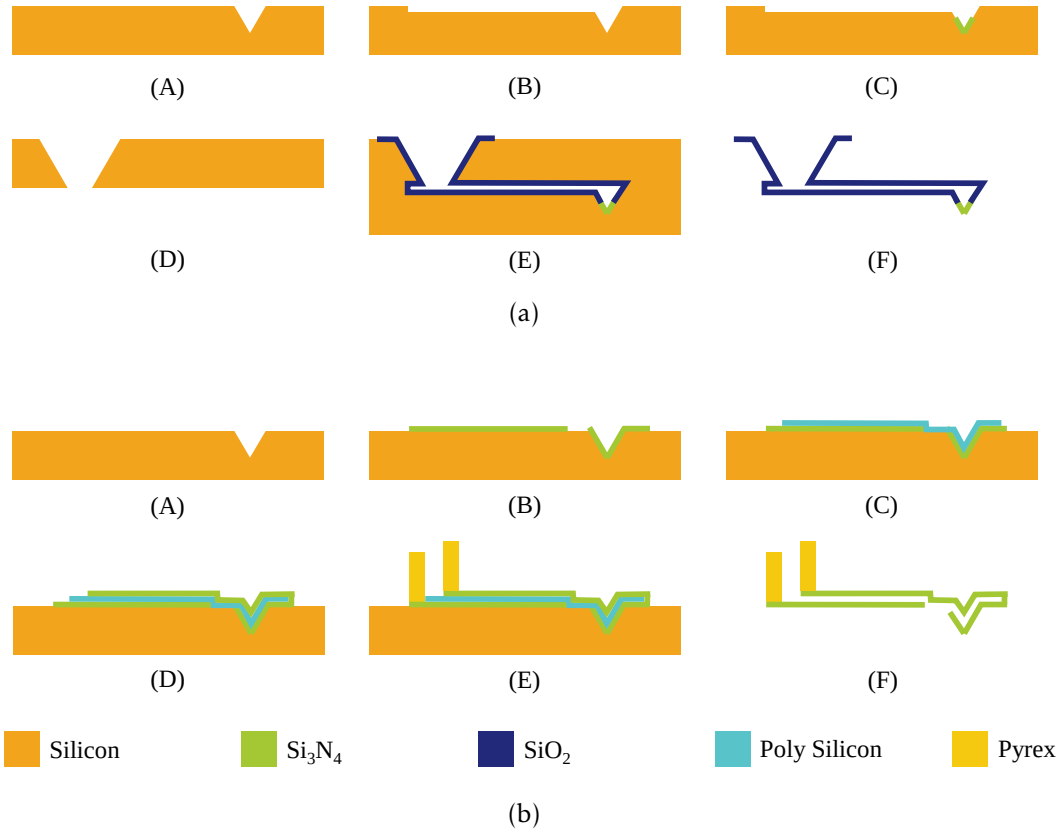

Figure 1.2: Fabrication approach to obtain microchanneled cantilevers through (a) a thermal bonding process and (b) a sacrificial layer process (Adapted from [14]).

The channels can either be defined by photolithography followed by reactive ion etching (RIE) or through anisotropic etching with KOH. The aperture in the apex can

either be done by corner lithography or FIB.

The sacrificial layer process (Figure 1.2b), in which the first microfountain pen and the fountain nanoprobe were fabricated, can be generalized to the following steps [14, 18, 19]: (A) Etching of an inverted pyramid on a <100> silicon wafer; (B) Deposition of a Si_3N_4 layer by Low Pressure Chemical Vapour Deposition (LPCVD) - to form the floor of the channels); (C) Deposition of a sacrificial layer (poly silicon or silicon dioxide) by LPCVD; (D) Deposition of a Si_3N_4 layer by LPCVD (to form the ceiling of the channels); (E) Bonding the two wafers with the reservoir; and (F) Etching of the polycrystalline silicon and of the silicon wafer.

Lithography followed by RIE define the channels' geometry and paths in each layer.

1.3 Thesis Outline

This dissertation describes the work performed at INESC-MN and AFMaRT-FCUL and it is divided in 5 chapters. The present one gives an overview of the state of the art, motivation and objectives of the dissertation project.

Chapter 2 describes Atomic Force Microscopy techniques together with the cantilever physics. The last section gives an insight into microfluidics physics.

Chapter 3 explains the equipment and techniques used during the cantilever fabrication and further characterisation.

Chapter 4 describes the fabrication processes, discusses and analyses the results obtained during the fabrication of the cantilever, highlighting their advantages and limitations together with the proposed solutions to possible issues.

Lastly, Chapter 5 does an overall discussion of the the work along with conclusions and considerations for the future.

Chapter 2

Theoretical Background

This chapter explains the working principles and operation modes of the Atomic Force Microscopy (AFM), with focus on the cantilever properties and characteristics. An introduction to some relevant concepts regarding the sample-tip interactions and microfluidics is also given.

2.1 Atomic Force Microscopy

In 1981, Dr Gerd Binning at the IBM Zurich Research Laboratory developed the Scanning Tunnelling Microscope (STM) which earned him the Nobel Prize in 1986. This instrument nowadays is capable of obtaining 3-D images of solid surfaces with atomic resolution. This technique is, however, limited to conductive surfaces since it uses the tunnelling of electrons as a working principle [20]. To overcome this limitation and enable the study of both conductive and isolating surfaces, the same team in 1985 developed the Atomic Force Microscope (AFM). Both STM and AFM are a type of scanning probe microscopy (SPM), where a probe scans a sample while interacting with it. These techniques have similar setup designs but, while the STM working principle is the tunnelling current sensed on the probe when close to the sample's surface, the AFM is based on the deflection of a cantilever probe when near the surface due to tip-sample force interactions [21].

The AFM setup and working principle of this technique are schematized in Figure 2.1. A cantilever beam is mounted on a holder which contains a piezoelectric transducer that can oscillate on the z-axis. An optical beam is directed at the end of the cantilever beam which is then reflected to an optical sensor. The sample is mounted on a platform containing piezoelectric transducers that move the sample in the x, y and z-directions. When the cantilever suffers a deflection, the optical beam path will also change. This shift is detected by the optical sensor, which will then send a signal to the platform. The platform will adjust the distance from the sample to the tip depending on the operation mode of the AFM [22]. The optical sensor gives an output in terms of voltage which needs to be converted to displacement. Having the piezoelectrics calibrated, this conversion is made through a force curve as shown in Figure 2.2a. Figure 2.2b shows the procedure

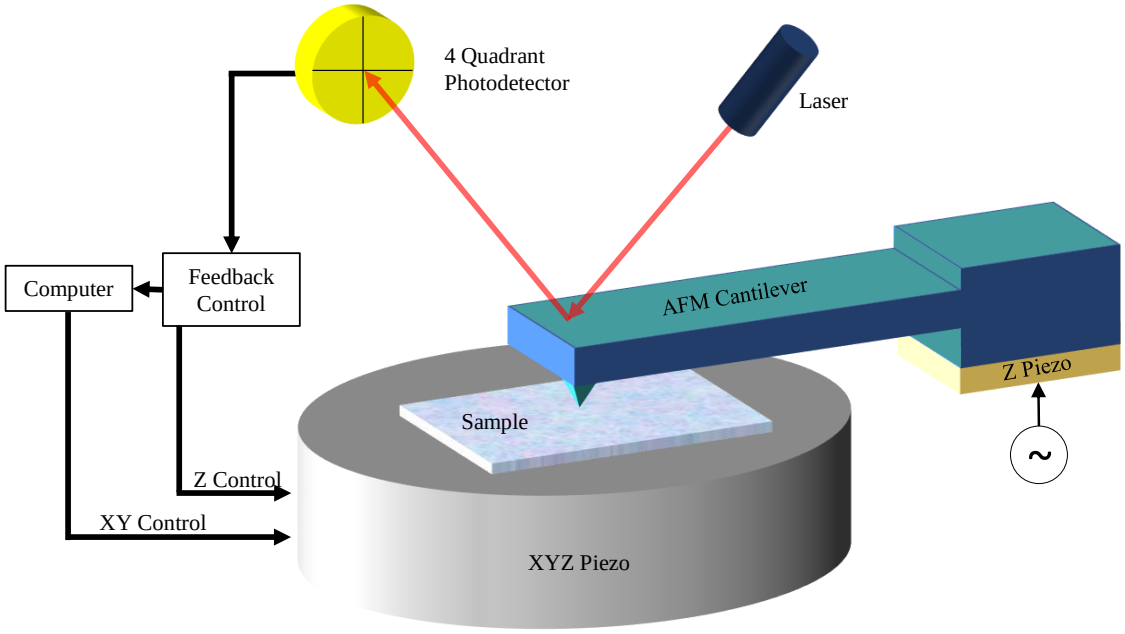

Figure 2.1: Schematic of an Atomic Force Microscope components and design.

for measuring this curve: The cantilever is far from the sample and does not suffer any bending (A). The cantilever then moves slowly down until it is near the sample; when they are close enough to each other, the attractive forces (Van-der-Waals and capillary forces in the air) overcome the cantilever spring constant and the cantilever snaps against the sample (B). In situation (C) the cantilever bends up as it continues to move to the sample, deflecting the optical beam across the sensor. Doing a linear fit it in this situation is possible to convert the voltage to displacement as long as the displacement of the transducer is known. After this, the cantilever moves in the opposite direction. To pull the cantilever from the sample (D-E) a bigger displacement is required compared to (B). This is due to adhesion forces. Depending on the air humidity and hydrophilicity of the tip and sample, these can form a capillary bridge that causes a strong adhesion.

The AFM can be operated either in static or dynamic mode. In static mode the tip at the end of the cantilever beam actually touches the sample surface, as explained earlier. The force F exerted on the cantilever obeys Hooke's law:

$$F = k\Delta z, \tag{2.1}$$

where Δz is the displacement from the initial position and k the spring constant that characterizes the cantilever.

Meanwhile, in dynamic mode the tip of the cantilever can either touch the sample or be a few nanometers away from it. In this mode the piezoelectric transducer on the cantilever holder oscillates along the z-direction, making the cantilever vibrate near its resonance frequency.

This dynamic mode can be explained by the harmonic model [22, 23]. The cantilever holder oscillates with an amplitude A_d and frequency ω. Without external or damping

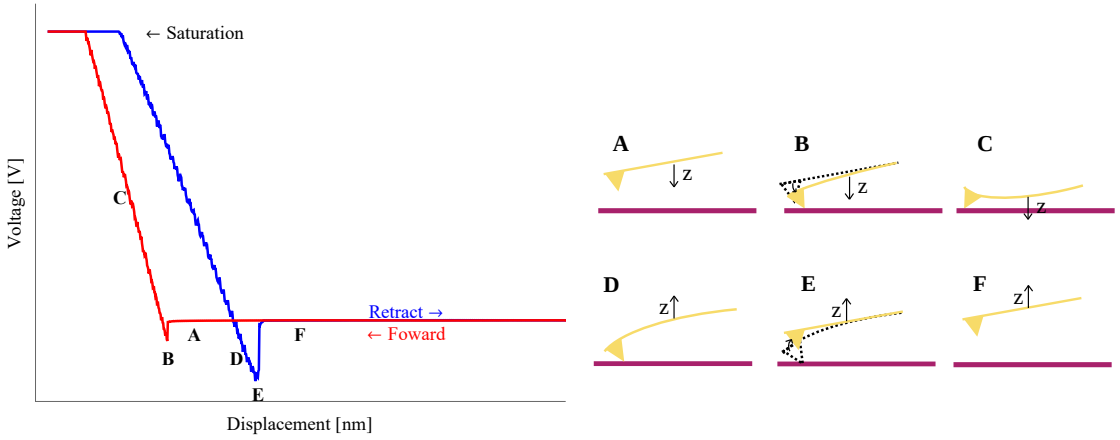

(a) (b)

Figure 2.2: (a) Typical force curve of the cantilever interacting with the substrate and (b) schematic of the interactions in different parts of the curve.

forces, the cantilever has a natural frequency ω_0, which depends on the stiffness constant k (which depends on the cantilever geometry and size) and its effective mass m^*

$$\omega_0 = \sqrt{\frac{k}{m^*}}. \tag{2.2}$$

Considering external forces, the cantilever oscillation can be explained by the damped harmonic oscillator:

$$m^*\ddot{z}(t) = -\alpha\dot{z}(t) - kz(t) + kz_d(t), \tag{2.3}$$

where α is the damping coefficient, $z_d(t)$ the displacement of the holder where the cantilever is mounted on. Since the holder is oscillating, $z_d(t) = A_d\cos(\omega t)$. Equation (2.3) can be rewritten in terms of the quality factor $Q = m^*\omega_0/\alpha$, which describes the number of oscillation cycles required for the oscillation amplitude to decay to $1/e$ of the initial amplitude after the external excitation is turned off.

$$\ddot{z}(t) + \frac{\omega_0}{Q}\dot{z}(t) + \omega_0^2 z(t) = A_d\omega_0^2\cos(\omega t). \tag{2.4}$$

When the excitation of the cantilever starts, it will reach a steady state after Q/π oscillation cycles, where the amplitude, phase and frequency are constant over time. This oscillation has an amplitude A_0 and a phase difference ϕ:

$$z_s = A_0\cos(\omega t + \phi). \tag{2.5}$$

Using Equation (2.5) in Equation (2.4), the amplitude and phase are given by

$$A_0 = \frac{A_d Q\omega_0 2}{\sqrt{\omega^2\omega_0^2 + Q^2(\omega_0^2 - \omega^2)^2}}, \tag{2.6}$$

$$\phi = \arctan\left(\frac{\omega\omega_0}{Q(\omega_0^2 - \omega^2)}\right). \tag{2.7}$$

The damping term of the harmonic oscillation causes the resonance frequency to shift from the natural frequency ω_0 to ω_0^*:

$$\omega_0^* = \omega_0 \sqrt{1 - \frac{1}{2Q^2}}. \tag{2.8}$$

When the AFM is operated in dynamic mode it can work either in non-contact mode

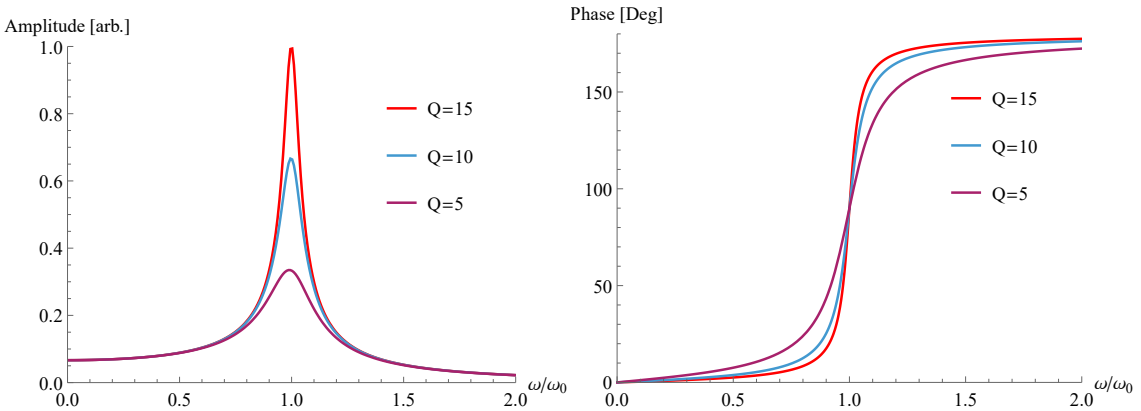

Figure 2.3: (a) Amplitude and (b) phase curves for a damped harmonic oscillator with different quality factors.

(NCM), where the cantilever tip does not come in contact with the sample, or in tapping/intermittent contact mode (ICM), where the tip taps the surface. Tapping mode, which is the most commonly used, uses amplitude modulation (AM-AFM). As the tip approaches the surface, the amplitude of the oscillation will decrease. The feedback controller contains a lock-in amplifier that receives the signal from the photo detector and determines its the amplitude and phase. A PID will use the difference between the amplitude from the lock-in and the set-point and send a signal to readjust the stage's z-position, keeping the cantilever's amplitude constant. Meanwhile, NCM uses frequency modulation (FM-AFM). Instead of a lock-in, the frequency is maintained constant through a phase-locked loop (PPL). These modes are shown in Figure 2.4a. For these dynamic methods, Q and f_{res} will limit the sample scanning speed. For example, in tapping mode, when the cantilever encounters a feature its amplitude does not change instantly (Figure 2.4b). The response time $\tau = Q/\pi f_{res}$ is the time it takes for the cantilever to reach a new equilibrium after perturbation. To obtain a faster scanning speed, f_{res} should be high and Q low.

Depending on the type of study and sample that will be analysed, one method can be more suitable than the other. Since these methods work with different proximities to the sample, the magnitude of the forces that the tip will be subjected to will also be different. These interactions have a similar profile as the van der Waals potential (Figure 2.5a) and, for each region, the cantilever properties must fulfil some parameters regarding k, ω and

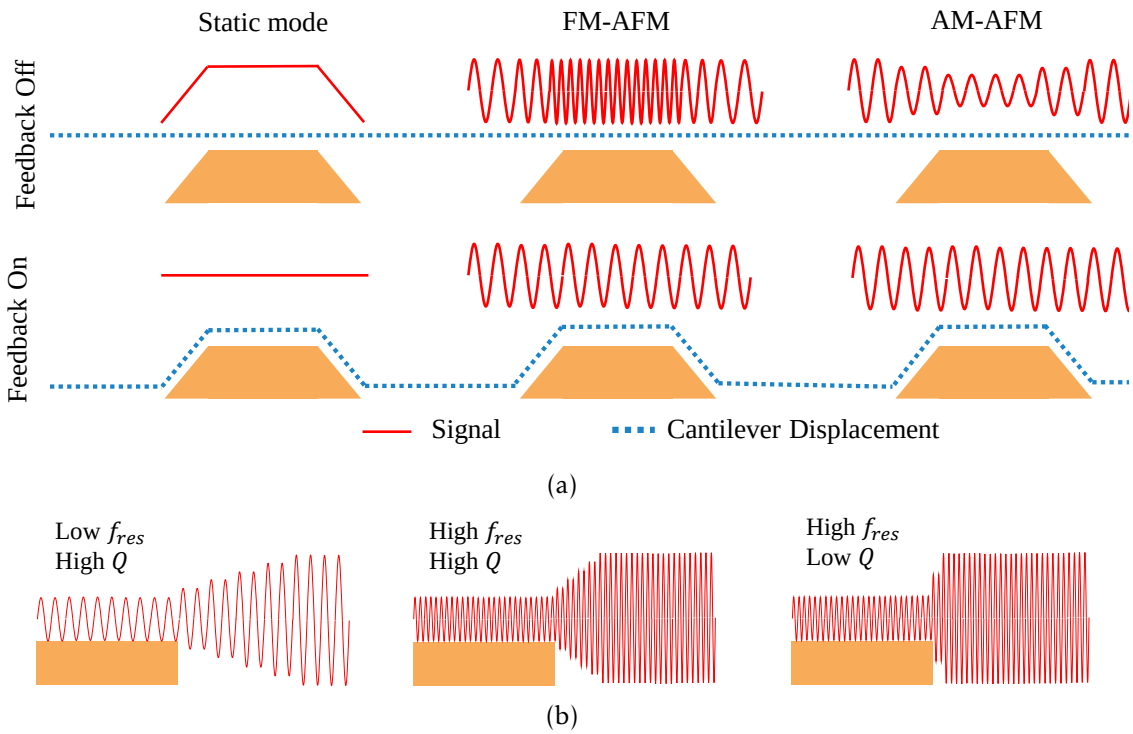

Figure 2.4: (a) Schematic of the obtained signals and displacement of the tip when it encounters a feature for the three type of modes: contact, frequency modulation, and amplitude modulation with and without feedback. (b) Schematic of the response time of a cantilever encountering a step for different Q and f in tapping mode (Reproduced from [24]).

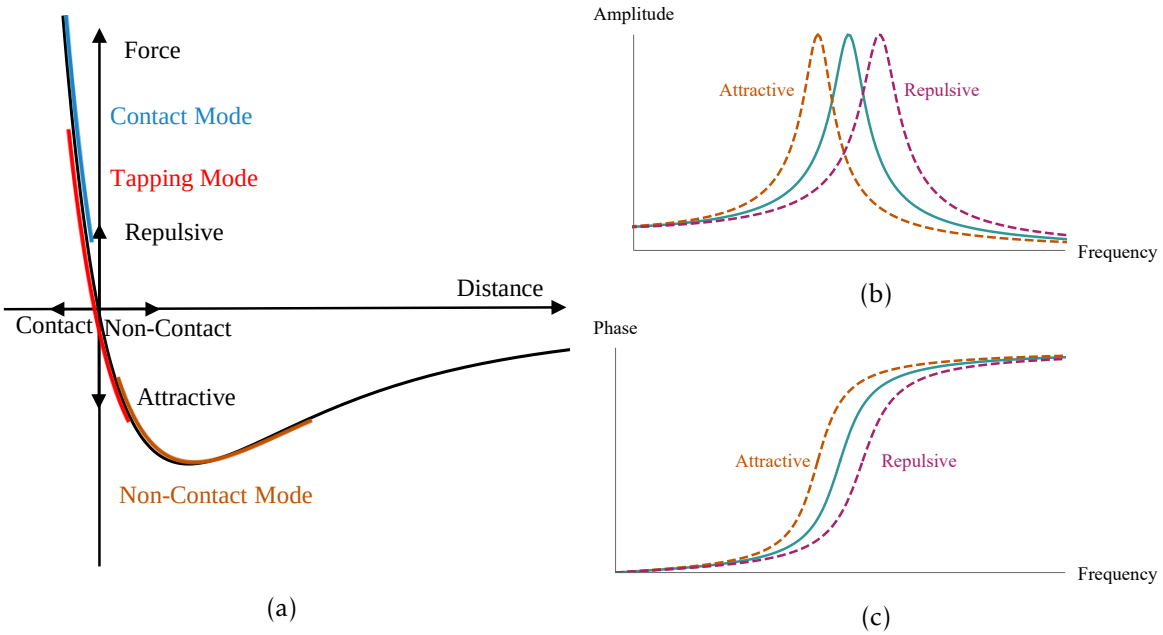

Figure 2.5: (a) Representation of the interaction regimes as the tip approaches the sample and the regimes for each mode and (b) response of the frequency and phase for attractive and repulsive interactions.

Q. For contact mode, the cantilevers have stiffness' between 0.1 – 1 N/m, for tapping mode between 1 – 10 N/m and for NCM between 10 – 100 N/m.

2.2 Cantilever Physics

As the tip of the cantilever approaches the substrate, it experiences a force which deflects the beam towards the substrate. This deflection can be characterized according to the Euler-Bernoulli beam theory when cantilevers are long and thin. The tip is usually at one end of the beam and centred along the width, so it can be assumed that the forces that it experiences can be a point load at the end of the beam. The bending of the beam due to normal load is described by the Euler equation [25, 26]:

$$M = EI\frac{d^2y}{dx^2}, \tag{2.9}$$

where M is the bending moment on the beam cross-section, I is the moment of inertia of the cross-section and E is the Young modulus.

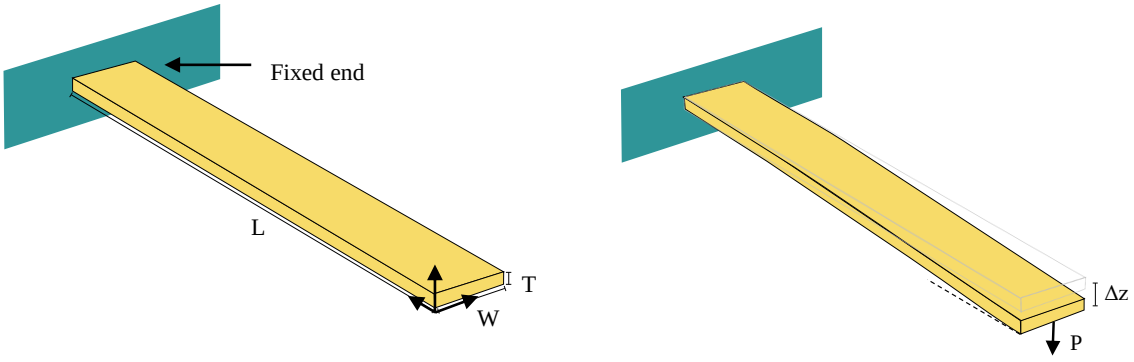

(a) (b)

Figure 2.6: Schematic of (a) a cantilever of length L with a load point P at $x = 0$ and (b) resulting deflection Δz of the beam.

Since there is a rigid connection at $x = L$, the boundary conditions are: $x = L$, $y = 0$ and $x = L$, $\theta = 0$. Applying these conditions while integrating Equation (2.9), the deflection in the beam is

$$\Delta z = \frac{1}{EI}\left(-\frac{Px^3}{6} + \frac{PL^2x}{2} - \frac{PL^3}{3}\right), \tag{2.10}$$

and the angle

$$\theta = \frac{1}{EI}\left(-\frac{Px^2}{2} + \frac{PL^2x}{2}\right). \tag{2.11}$$

The deflection of the beam is only relevant at $x = 0$, which leads to:

$$\Delta z = -\frac{PL^3}{3EI}. \tag{2.12}$$

As referred before, the cantilever beam can be described as a spring, which has a stiffness constant k, given by

$$k = \frac{P}{\Delta z} = \frac{EI}{L^3}. \tag{2.13}$$

For a cantilever with a rectangular cross-section of width W and thickness T, the inertia is

$$I = \frac{WT^3}{12}, \tag{2.14}$$

which leads to a stiffness constant of rectangular cantilever beams of

$$k = \frac{EWT^3}{4L^3}. \tag{2.15}$$

As the tip of the cantilever moves across the sample, the frictional forces will cause a lateral and consequently a torsional deflection of the cantilever [27]. The lateral spring constant k_{lat} is given by

$$k_{lat} = \frac{ETW^3}{L^3} = \frac{W^2}{T^2}k. \tag{2.16}$$

Assuming a tip with a height h_{tip}, the torsional stiffness is

$$k_{tor} = \frac{GWT^3}{3Lh_{tip}^2}, \tag{2.17}$$

where $G = E/2(v+1)$ is the modulus of rigidity and v the Poisson ratio.

The resonance frequency is also obtained from the Euler-Bernoulli equation [23, 28]:

$$\frac{d^2}{dx^2}\left(EI\frac{d^2y}{dx^2}\right) = p(x). \tag{2.18}$$

For a vibrating beam, an harmonic motion $p(x) = \rho\omega^2 y$ is assumed, where ρ is the mass per unit length of the beam. Equation (2.18) becomes:

$$EI\frac{d^4y}{dx^4} - \rho\omega^2 y. \tag{2.19}$$

Defining $\beta = \rho\frac{\omega^2}{EI}$, Equation (2.19) becomes a fourth-order differential equation:

$$\frac{d^4y}{dx^4} - \beta^4 y = 0. \tag{2.20}$$

A solution to this differential equation is a superposition of normal modes with the position-dependent and time-dependent variables separated:

$$y(x,t) = \sum_{n=1}^{\infty} Y_n(x)\cos(\omega t), \tag{2.21}$$

where $Y_n(x)$ can be written as

$$Y_n(x) = A_n\cosh(\beta_n x) + B_n\sinh(\beta_n x) + C_n\cosh(\beta_n x) + D_n\sinh(\beta_n x). \tag{2.22}$$

Applying the boundary conditions for the cantilever

$$Y_n(L) = \frac{\partial}{\partial x} Y_n(L) = \frac{\partial^2}{\partial x^2} Y_n(0) = \frac{\partial^3}{\partial x^3} Y_n(0) = 0. \tag{2.23}$$

This leads to a system of linear equations of fourth order, for which the solution for a determinant equal to zero is:

$$\cos(\beta L)\cosh(\beta L) + 1 = 0. \tag{2.24}$$

Equation (2.24) is satisfied by a number of values βL that correspond to each mode of oscillation, these are namely $\lambda_n = \beta_n L$= 1.8751, 4.6941 and 7.8548 for the first 3 modes.

The resonance frequencies for a rectangular cantilever are therefore:

$$\omega_n = \frac{\lambda_n^2}{2\sqrt{3}} \frac{T}{L^2} \sqrt{\frac{E}{\rho}}. \tag{2.25}$$

Cantilever with a hollow rectangular section

For a rectangular cantilever with a hollow rectangular section of height t_c and width w_c the moment of inertia is:

$$I = \frac{1}{12} W T^3 - \frac{1}{12} w_c t_c^3. \tag{2.26}$$

Substituting Equation (2.26) in Equation (2.13), the stiffness constant for a cantilever with a hollow rectangular section is the stiffness constant of the cantilever without the hollow part;

$$k = \frac{E}{4L^3}[W T^3 - w t^3]. \tag{2.27}$$

Analogous to a capacitor in an electric circuit, the resulting stiffness constant k_{eq} of a cantilever with parallel beams is:

$$k_{eq} = k_1 + k_2. \tag{2.28}$$

While in series it is given by:

$$k_{eq} = \left(\frac{1}{k_1} + \frac{1}{k_2} \right)^{-1}, \tag{2.29}$$

where k_1 and k_2 are the stiffness constant of each beam.

The cantilevers used in AFM should have a low normal spring constant, a high lateral spring constant, a high resonant frequency, a high quality factor, short cantilever length, a sharp probing tip and should have a reflective layer on top to enhance the reflected signal [29].

The AFM cantilevers may have a variety of tip geometries that can be obtained through different fabrication methods. The tip at the end of the beam will contribute with an extra mass which will cause a negative shift of the resonance frequency as expected from Equation (2.2). Due to the different geometries, materials, and coatings that can be used on a cantilever, its properties will vary slightly from the expected behaviour given by the analytical expressions. Finite element methods are used to get a more approximate value.

Comsol Analysis

Several cantilever structures were considered for fabrication: a simple rectangular cantilever beam (Figure 2.7a), and second version with an arrow-shaped end (Figure 2.7d); a cantilever with two parallel beams (Figure 2.7b); a hollow channel cantilever (Figure 2.7e); and a simple rectangular beam with two hollow tips at the end (Figure 2.7c and 2.7f), obtained from a KOH etch.

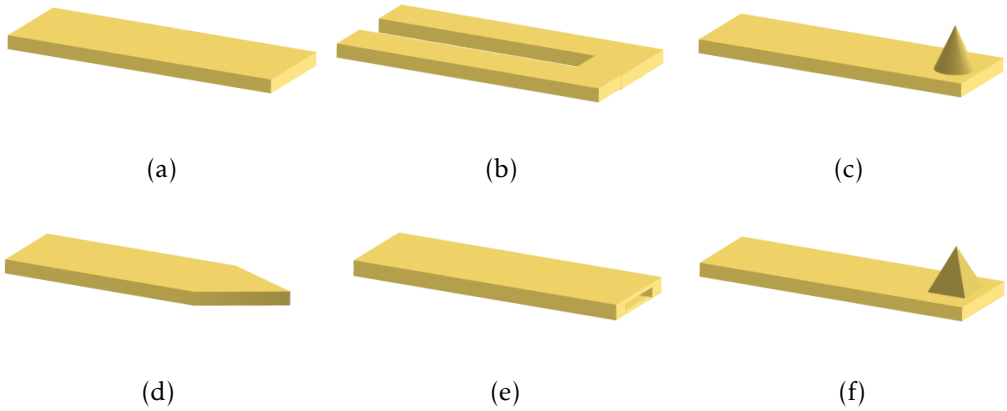

Figure 2.7: Cantilever geometries.

Silicon nitride cantilevers with a rectangular cross-section and constant width (Figure 2.7a) were dimensioned so the stiffness constant falls between 0.2 and 10 N/m, and for a resonance frequency between 10 kHz and 500 kHz. The cantilever thickness is 0.5 µm, and the width and length were chosen according to the requisites (Figure 2.8).

This structure was analysed through finite element analysis using the COMSOL Multiphysics software with the Eigenfrequency study. Equation (2.25) gives a good approximation for the resonance frequency when the cantilever is slender ($L >> T$). Very long cantilevers may not sustain its own weight and are more prone to break during the fabrication. In Figure 2.9a, it is shown that the relative error between the expected and the simulated resonance frequency increases with the length of the cantilever. Although Equation (2.25) does not present a dependency with the cantilever's width, the simulated value diverges more with thinner cantilevers. It was tested if the mesh size would alter this values but it was not the case (Figure 2.9b).

The same resonance frequency as for the single beam is expected for the cantilevers with parallel beams, since Equation (2.25) does not present a dependency on the width. However, the connection between the beams adds mass at the end to the cantilever, the more the beams are separated apart, more mass is added (Figure 2.10b), thus the resonance frequency will be smaller. As for the cantilevers with the arrow end, since part of the cantilever was removed, it is expected an increase in the resonance frequency (Figure 2.10a). For both geometries, the shift is smaller for bigger lengths and widths since the removed/added mass becomes smaller relative to the mass of the whole structure.

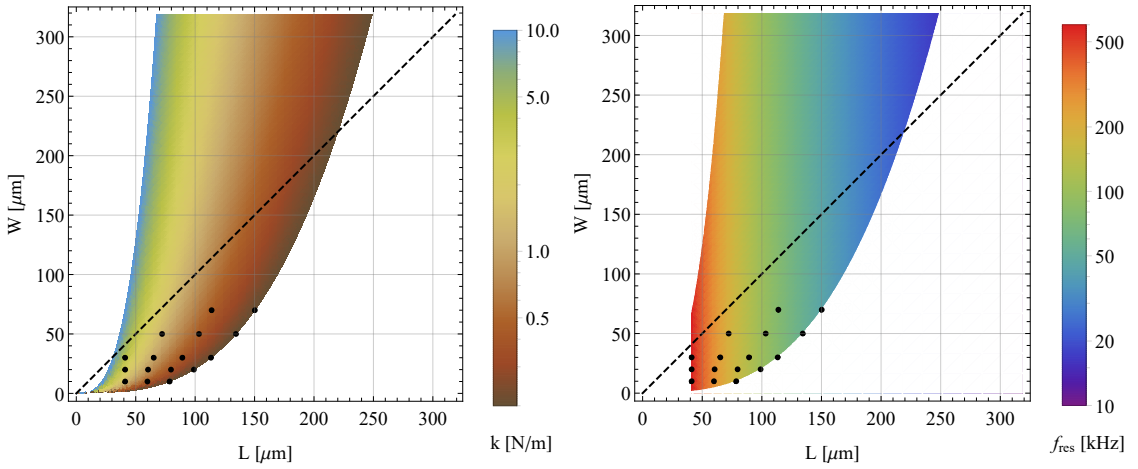

(a) (b)

Figure 2.8: (a) Length and width dimensions for a k between 0.2 and 10 N/m for a thickness of 0.5 µm and (b) respective resonance frequencies for those dimensions for a Si_3N_4 cantilever. The points are the chosen dimensions for the requisites with $L > W$.

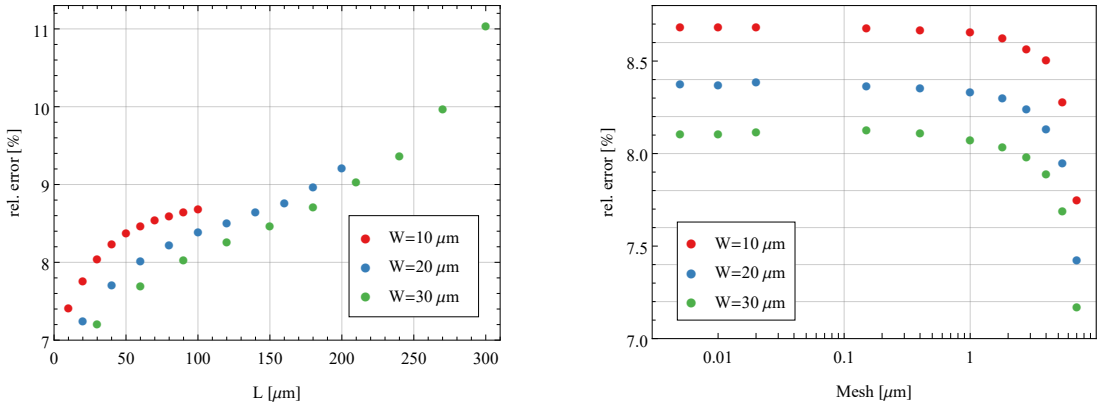

(a) (b)

Figure 2.9: (a) Relative error between the expected and simulated resonance frequency for different lengths for a Si_3N_4 cantilever of thickness 0.5 µm. (b) Influence of the mesh size on the calculated value.

As expected from Equation (2.2), adding a tip (pyramidal or conical) to the cantilever results in adding mass to the structure and thus a negative shift in the resonance frequency (Figure 2.11b), the bigger the tip the more mass is added. The resonance frequency for the hollow structure can be calculated using Equation (2.2), where k is obtained through Equation (2.27) and the effective mass is from the solid part of the structure. In Figure 2.11a the used analytical expression is coincident with the FEM points with relative errors below 2%. The dimensions chosen for the simulations were $T = 2.5$ µm, $t_c = 0.5$ µm and the L and W are the same as for the regular cantilever. w_c varies between 2 and 8 µm, but no significant change is verified in the resonant frequency. For these dimensions, the Reynolds Number falls between 10^{-6} and 10^{-7}, which ensures a laminar flow inside the cantilever.

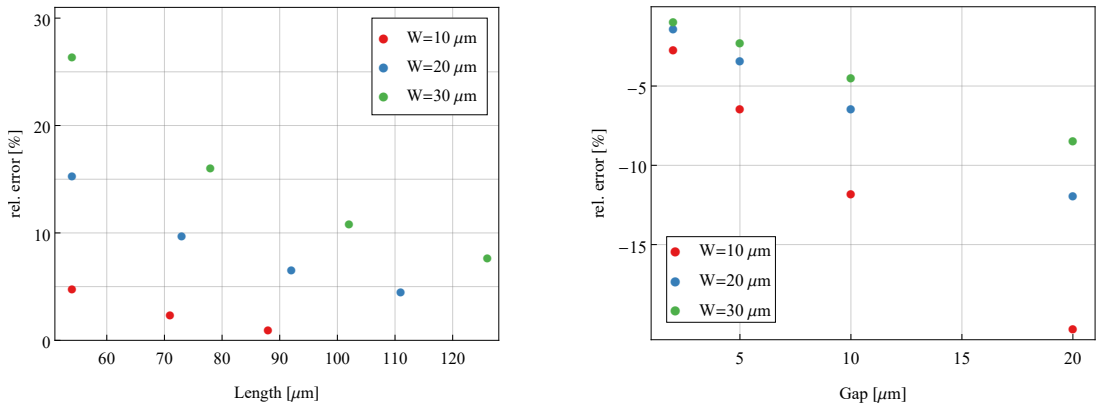

(a) (b)

Figure 2.10: Relative error of the resonance frequency between (a) the regular cantilever and the cantilever with an arrow end with thicknesses of 0.5 µm and (b) the regular cantilever and the cantilever with two parallel beams of length 54 µm and thickness 0.5 µm.

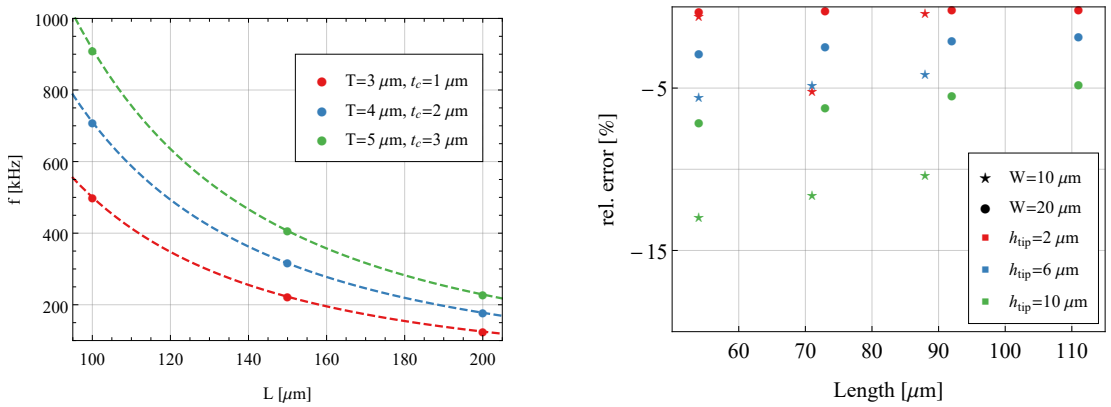

(a) (b)

Figure 2.11: (a) Resonance frequencies for a Si_3N_4 hollow cantilever with $W = 10$ µm and $w_c = 8$ µm and (b) relative error of the resonance frequency between the regular cantilever and the cantilever with a conical tip with thickness's of 0.5 µm.

2.3 Microfluidic Physics

In a microfluidic strucuture, the fluid behaviour will be dominated by viscous interactions with the surface since there is a higher area-to-volume ratio. The behaviour of a fluid inside a channel can be described by its Reynolds number (R_e). It defines two regimes: $R_e > 2000$ where the flow is turbulent, and $R_e < 2000$ where the flow is laminar. For micrometric channels the Reynolds number becomes small ($R_e << 1$) and the flow is laminar [11, 30, 31]. It is defined as:

$$R_e = \frac{2R\rho v}{\eta}, \tag{2.30}$$

where R is the channel radius, ρ the fluid density, v the mean fluid velocity and η the dynamic viscosity. For rectangular channels, R is $2A_c/P_c$ where A_c is the cross-section area

and P_c the perimeter. Solving the Navier-Stokes equation (Equation (2.31)) for a driven, steady and laminar flow, the equation reduces to Equation (2.32):

$$\frac{\partial \mathbf{v}}{\partial t} + (\mathbf{v} \cdot \nabla)\mathbf{v} = \mathbf{g} - \frac{1}{\rho_0}\nabla p + v\nabla^2 \mathbf{v}, \tag{2.31a}$$

$$\nabla \cdot \mathbf{v} = 0, \tag{2.31b}$$

$$\nabla p = \eta e_z \nabla^2 v_z(r). \tag{2.32}$$

(a) (b)

Figure 2.12: Poiseuille velocity profile in a channel with a (a) circular and (b) rectangular cross-section.

Solving Equation (2.32) by applying no slip boundary conditions, for a circular channel it results in a parabolic profile (Figure 2.12), described by

$$v_z = \frac{\Delta p}{L}\frac{1}{4\eta}(R^2 - r^2), \tag{2.33}$$

where Δp is the pressure drop along the length L of the channel. The volumetric discharge is obtained by the Hagen-Poiseuille law where the volume carried through the channel along the time is obtained by integrating the velocity field over the channel's cross-section:

$$\int_0^R v_z(r) 2\pi r dr = \frac{\Delta p}{L}\frac{\pi R^4}{8\eta}. \tag{2.34}$$

Rectangular channels are also obtained due to some microfabrication techniques. For a rectangular cross-section there is no analytical solution for Equation (2.32). Using Fourier expansion and assuming a width bigger than the height ($W > T$) the flow rate is:

$$Q \approx \frac{T^3 W \Delta p}{12\eta}\left[1 - 0.63\frac{T}{W}\right]. \tag{2.35}$$

For a rectangular cross-section channel, the capillary force is given by the component along the tube of the perimeter times the interfacial tension:

$$F = 2(W + T)\sigma\cos(\theta_c), \tag{2.36}$$

where σ is the interfacial tension and θ_c the contact angle which determines the hydrophilicity of the surface [5, 32]. The capillary force can be expressed as a pressure by dividing the force by the cross-section:

$$P_{cap} = \frac{F}{A} = \frac{2(W + T)\sigma\cos(\theta_c)}{WT} = 2\sigma\cos(\theta_c)\left(\frac{1}{W} + \frac{1}{T}\right). \tag{2.37}$$

Depending on the pumping mechanism, the flow rate on a channel will be limited either by the pressure drop over the fluidic system or by capillary pressure.

Chapter 3

Experimental Methods

This chapter presents the proposed processes for the fabrication of the cantilever and the techniques and equipment operated. The monitorisation methods used during the fabrication and characterisation methods utilised after obtaining the cantilever are also explained. For each technique, the process is described together with the equipment parameters. The cantilever fabrication and simultaneous characterisation were performed at Instituto de Engenharia de Sistemas e Computadores – Microsistemas e Nanotecnologias (INESC-MN) facilities, while the further characterisation was performed at Laboratório de Microscopia de Força Atómica e Técnicas Relacionadas (AFMaRT), FCUL.

3.1 Fabrication Equipment and Techniques

To fabricate the cantilever it is required a clean-room environment to avoid sample contamination. This is a room with controlled temperature, air pressure, humidity, vibration and light. INESC-MN possesses a class 10 (yellow area), a class 100 (white area) and a class 10000 (grey area), this classification regards the quantity of dust particles larger than 1 µm per cubic feet of air.

3.1.1 Photolithography

The patterning of the cantilever features and its measurements, such as the length and width, are first defined in a polymer which is photosensitive, and then transferred to the substrate. This process can be defined in separate steps, namely:

Vapor Prime

The photoresist (PR) adhesion to the substrate is improved by removing the adhered water on the surface and treating it with hexamethyl disilizane (HMDS). HDMS is applied in gas form and makes the surface hydrophobic thus ensuring a good photoresist-to-wafer adhesion.

Table 3.1: Vapor Prime Parameters.

Step Description	Conditions
Wafer dehydration	Vacuum, 10 Torr, 2 min. N2 inlet, 760 Torr, 3 min. Heating to 130 ºC
Priming	Vacuum, 1 Torr, 3 min. HDMS, 6 Torr, 5 min.
Purge prime exhaust	Vacuum, 4 Torr, 1 min. N2 inlet, 500 Torr, 2 min. Vacuum, 4 Torr, 2 min.
Return to atmosphere	N2 inlet, 3 min.

Coating

The sample is mounted on a wafer holder and the PR is dispensed in a liquid form on top of the sample. Then the sample spins at 2500 rpm for 30 seconds spreading the PR across the wafer resulting in a thickness of 1.45 µm. Afterwards, the sample undergoes a soft bake at 85 ºC for 60 seconds to evaporate the solvents, leaving the PR molecules behind. This process occurs in a Silicon Valley Group (SVG) track – Figure 3.1a.

Exposure

The PR used was PFR7790G-27cP which is a positive resist, meaning that the resist becomes soluble to a developer after being exposed to a certain wavelength. The sample is exposed with the Heidelberg DWL 2.0 which has a 440 nm diode laser, Figure 3.1b. For a first lithography, the alignment system aligns the sample with the exposure system by providing it with the location of the two bottom corners of the sample. For a second lithography, the system is aligned using alignment marks which are printed on the first lithography. The masks were exposed with a 5 mm offset both horizontally and vertically from the bottom left corner of the sample. The laser scans the sample, only exposing the desired parts that are specified through a CAD file as shown in Figure 3.1c.

Development

After the exposure, the sample undergoes a bake for 60 s at 110 ºC in order to prevent more reactions due to standing light waves on the PR. The sample is then rinsed with water and with the developer (TMA238WA) which dissolves the PR in the exposed areas. Lastly, the sample is rinsed with water while spinning to remove the exposed PR from the sample.

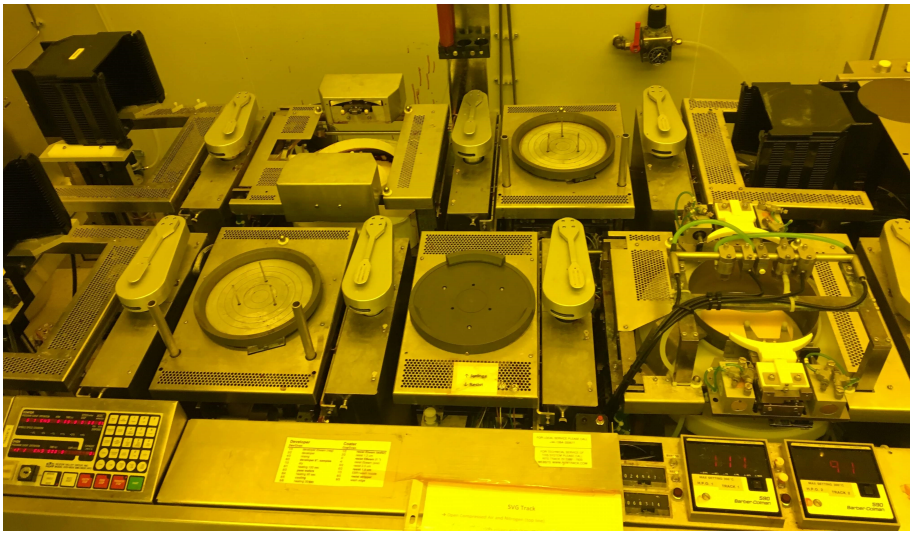

(a)

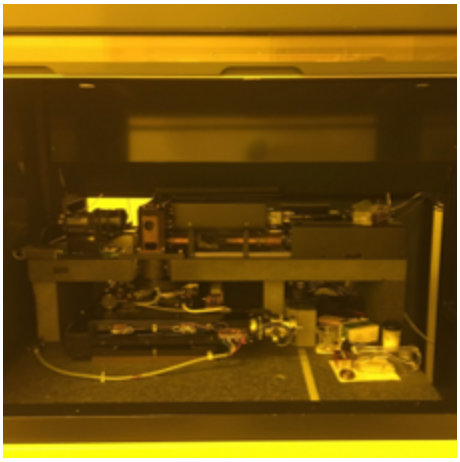

(b)

(c)

Figure 3.1: (a) SVG track, (b) Heidelberg DWL 2.0 and (c) cantilevers drawn in CAD.

3.1.2 Reactive Ion Etching

After the photolithography, the pattern must be transferred to the substrate. In this step, the features that are covered with PR remain on the sample while the others are etched away. In this process, Si_3N_4 and SiO_2 are removed by reactive ion etching through the LAM Research Rainbow Plasma Etcher 4400 (Figure 3.2b). The sample enters a vacuum chamber and a chemically reactive plasma is created using an RF antenna. The generated reactive species are then accelerated against the sample and the sample material is removed both by chemical affinity and by sputtering due to the transfer of momentum of the reactive species (Figure 3.2a). The surface material, which suffers collisions with the ions, becomes reactive (i.e., dangling bonds at the surface) and the reactive species only interact with these. The recipes to remove these materials are described in Table 3.2 when these are deposited by the Oxford Instrument PECVD. This process can be monitored by a profilometer, microscope or visually, since these materials present different colours for

different thicknesses. The etch is completed when the grey colour of silicon is visible.

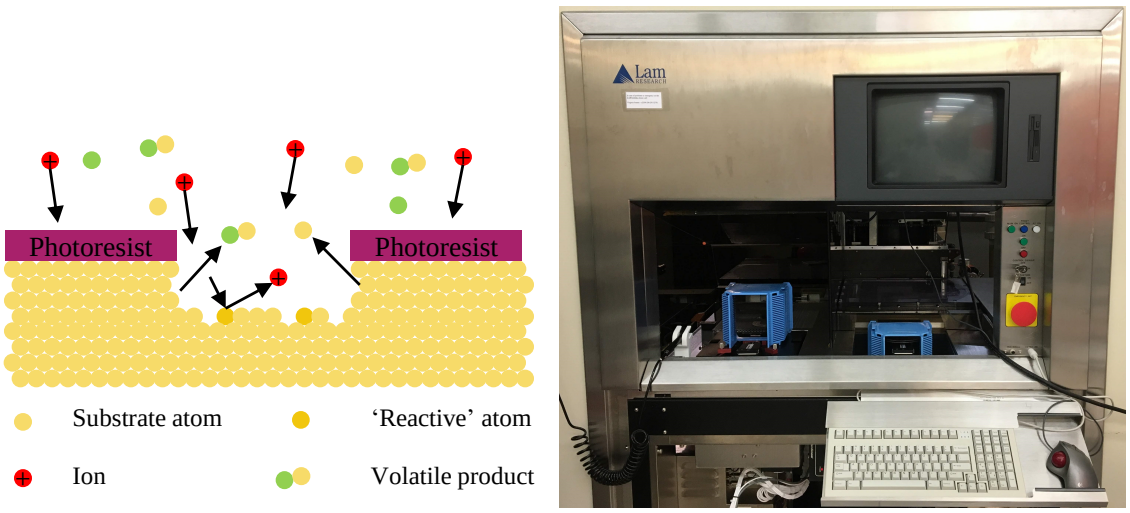

(a) (b)

Figure 3.2: (a) Representation of the etching mechanism for the reactive ion etching and (b) picture of the LAM Research Rainbow Plasma Etcher 4400.

Table 3.2: Etching parameters of the LAM Research Rainbow Plasma Etcher 4400.

	Power (W)	**Base Pressure (mTorr)**	**SF_6 flow (sccm)**	**$CHCF_3$ flow (sccm)**	**Ar flow (sccm)**	**CF_4 flow (sccm)**	**Etch Rate (nm/min)**
Si_3N_4	100	100	50	50	—	—	86.25
SiO_2		140	—	—	200	100	40

3.1.3 KOH Wet Etch

The silicon is etched using a solution of potassium hydroxide (KOH). A solution of 28% (m/m) of KOH was obtained by dissolving 98.8 g of 85% (m/m) of KOH into 201.2 g of water. To etch a thickness higher than 100 µm, the solution is kept at 80 ºC, resulting in a 1.45 µm/min etch rate [33]. To etch thicknesses lower than 10 µm, the solution temperature is kept at 60 ºC, which results in a lower etch rate of 0.5 µm/min (Figure 3.3b), so it is possible to have a more controlled and easy monitorisation of smaller feature sizes. The KOH bath is placed on top of a vibratory plate at 375 rpm and every 30 min the sample is taken out of the bath in order to refill with 20 mL of KOH. Each time the sample is taken out and the bath refilled, the temperature of the bath is measured to ensure the desired temperature is reached before placing the sample back in. The silicon crystalline orientation planes for a (100) silicon wafer are presented in Figure 3.4a, and the resulting shapes from the etch of the features drawn on the [100] plane is shown in Figure 3.4b.

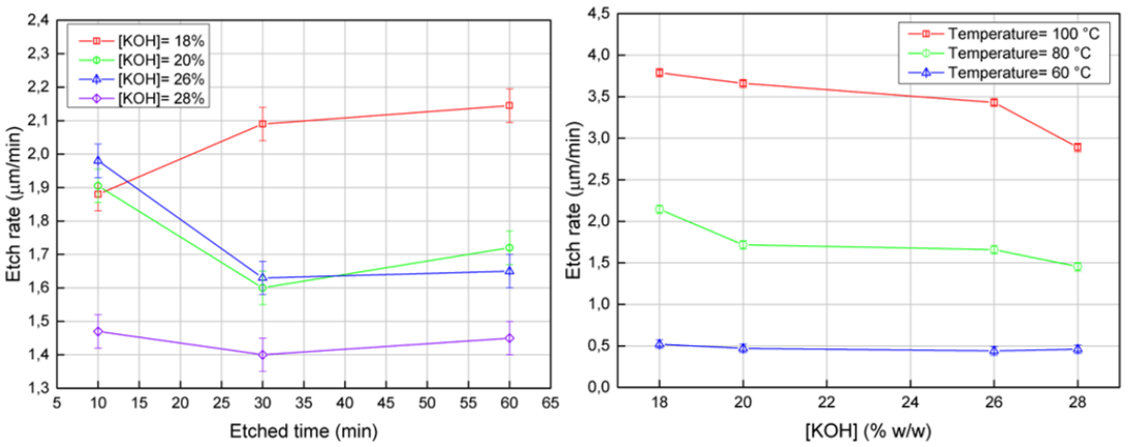

(a) (b)

Figure 3.3: (a) Etch rate versus etched time for the KOH wet etch process at 80°C for different KOH solution concentrations and (b)etch rate versus KOH concentration at different temperatures (Adopted from KOH etch protocol from INESC-MN).

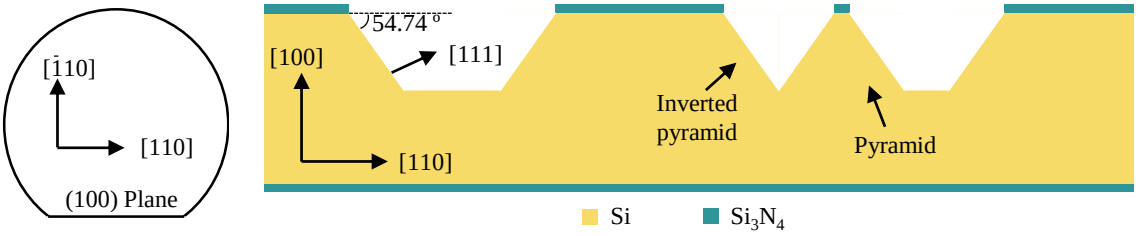

(a) (b)

Figure 3.4: (a) Schematic of a (100) silicon wafer and its crystalline planes and (b) profile view of the anisotropic silicon etch.

3.1.4 Magnetron Sputtering

Chromium, titanium and gold present a low (almost non-existent) etch rate with KOH [33]. These materials are used to protect the silicon from being etched by the KOH and allow the study of the sample with SEM. These materials are deposited using the Alcatel SCM 450 (Figure 3.5b). The Alcatel is composed of only one deposition chamber which requires 12 h of venting and pumping between batches to reach a base pressure of 10^{-5} Torr. The Alcatel deposits thin films through the transfer of momentum between the plasma ions and the target material. The plasma is created by applying a certain voltage to a gas which becomes ionised and then accelerated against the target. The system contains magnets behind the target that restrict the electrons' trajectory, confining them near the target. These electrons can ionize more atoms and thus generate higher deposition rates. Since some of the atoms removed from the target are neutral, they will not be affected by the magnetic field and will reach and be deposited on the substrate (Figure 3.5a). The deposition parameters for these materials are presented in Table 3.3.

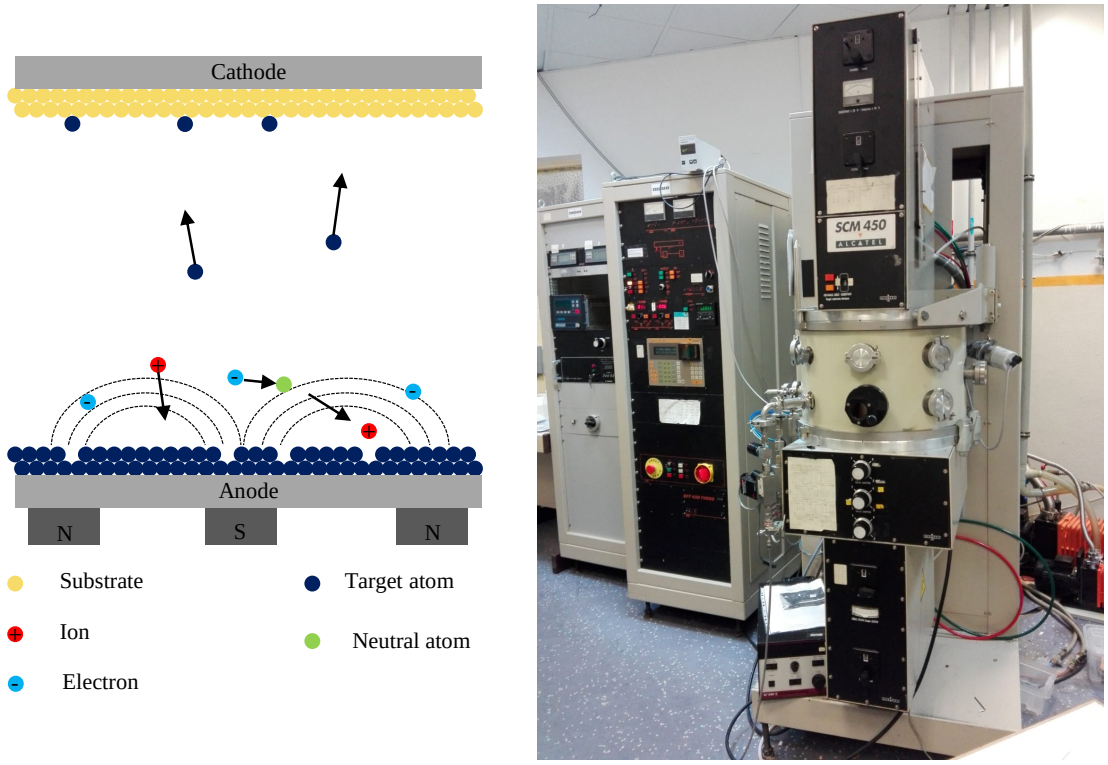

(a) (b)

Figure 3.5: (a) Schematic of the processes of magnetron sputtering and (b) Alcatel SCM 450.

Table 3.3: Deposition Parameters of the Alcatel SCM 450.

	Base Pressure (Torr)	**Ar Flow (sccm)**	**Working Pressure (mTorr)**	**Power**	**Deposition Rate (Å/s)**
Au			2.60	20 W_{DC}	0.69
Ti	1.1×10^{-6}	20	2.65	20 W_{RF}	0.46
Cr			2.63	20 W_{DC}	0.66

3.1.5 Plasma Enhanced Chemical Vapor Deposition

Plasma Enhanced Chemical Vapor Deposition (PECVD) enables the deposition of thin films with a good conformity (ratio of vertical to horizontal growth, Figure 3.6a). In this process, the thin films are deposited by exposing the wafer to volatile precursors which contain all the necessary components of the desired film material. The precursors decompose via thermal energy and through the collisions with the ions of the plasma, reacting with each other and depositing on the wafer surface (Figure 3.6b). The deposition of Si_3N_4 and SiO_2 is performed by the Oxford Instruments PECVD (Figure 3.6c). The deposition parameters for these materials are described in Table 3.4.

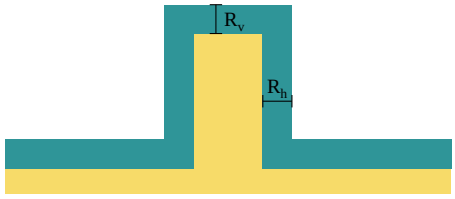

(a)

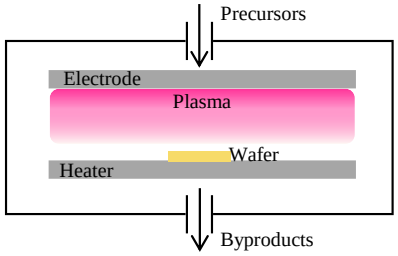

(b)

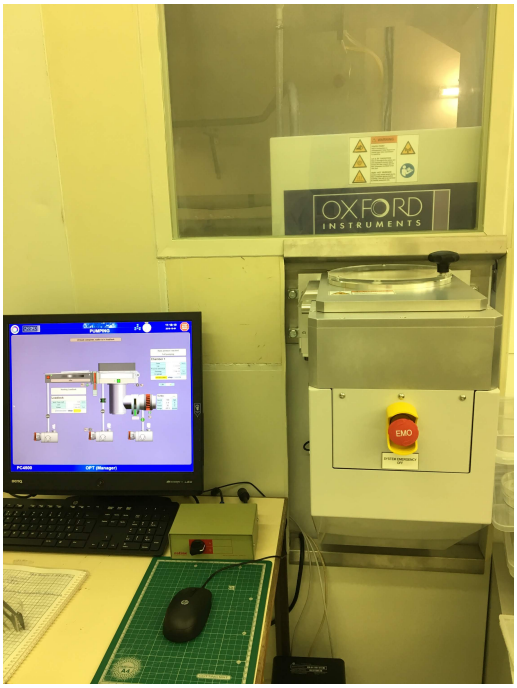

(c)

Figure 3.6: (a) Schematic of a deposition profile with a good conformity, (b) schematic of the CVD principle and (c) picture of the Oxford Instruments.

Table 3.4: Deposition parameters of the Oxford.

	Temperature (°C)	**Chamber Pressure (mTorr)**	**N_2 flow (sccm)**	**NH_3 flow (sccm)**	**SiH_4 flow (sccm)**	**N_2O flow (sccm)**	**Deposition Rate (nm/min)**
Si_3N_4	300	1000	980	20	20	—	16
SiO_2	350	1000	161.5	—	8.5	710	78

3.2 Monitorisation Methods of the Fabrication

3.2.1 Profilometer

A profilometer was used to measure the thickness of the deposited materials and of the etched thickness during physical and wet etches. The profilometer used was the Dektak 3030ST which consists of a diamond-tipped stylus connected to a piezoelectric sensor. The tip approaches the sample's surface and the sample holder moves in one direction. The surface topography is then measured by the vertical displacement of the tip across one scan.

3.2.2 Optical Microscope

An optical microscope is used to control the features' size and progress across the process. Together with an image processing software (ImageJ) some parameters, such as the

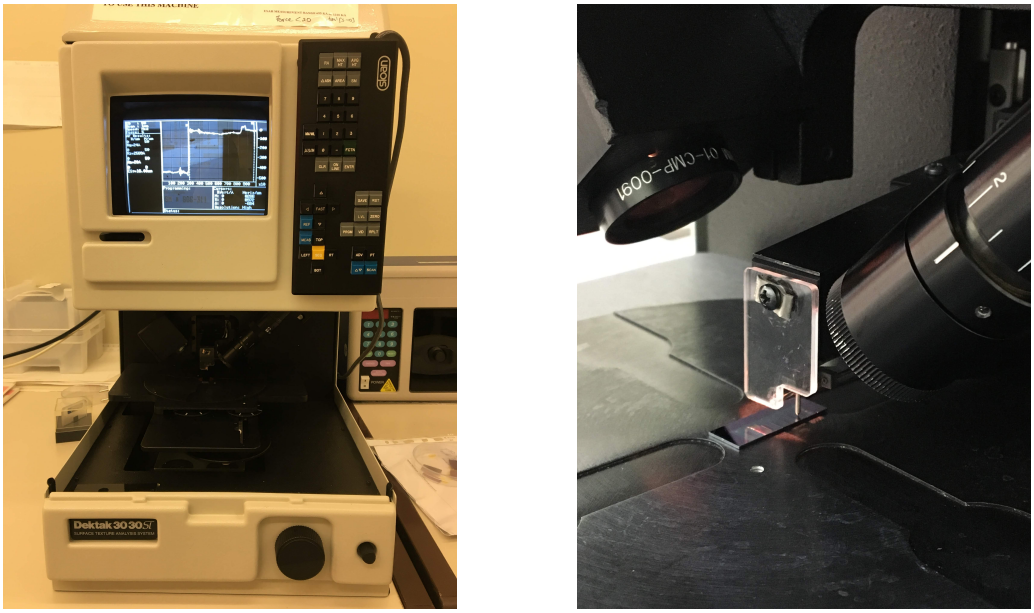

(a) (b)

Figure 3.7: (a) Dektak 3030ST and (b) stylus scanning a sample.

undercut caused on the Si_3N_4 by the KOH etch, is measured. The calibrated resolutions for different magnifications for a 2048x1536 image is shown in Table 3.5.

Table 3.5: Calibrated resolution for different magnifications for a 2048x1536 image.

Maginification	Scale (pixel/µm)
10x	2.604169
50x	12.84722
100x	25.50020

3.2.3 Scanning Electron Microscopy

After the deposition of the metallic layer on the sample, it is possible to view the structures with a Scanning Electron Microscopy (SEM). The SEM used is the S-2500 Scanning Electron Microscope, Figure 3.8a. The SEM scans the sample with a focused electron beam which interacts with the sample. The secondary electron emitted by the atoms of the sample are then collected and counted by a detector which enables the formation of an image. The SEM allows for a topographical view of the sample being scanned, Figure 3.8b. Together with image analysis software several dimensions can be analysed through this method.

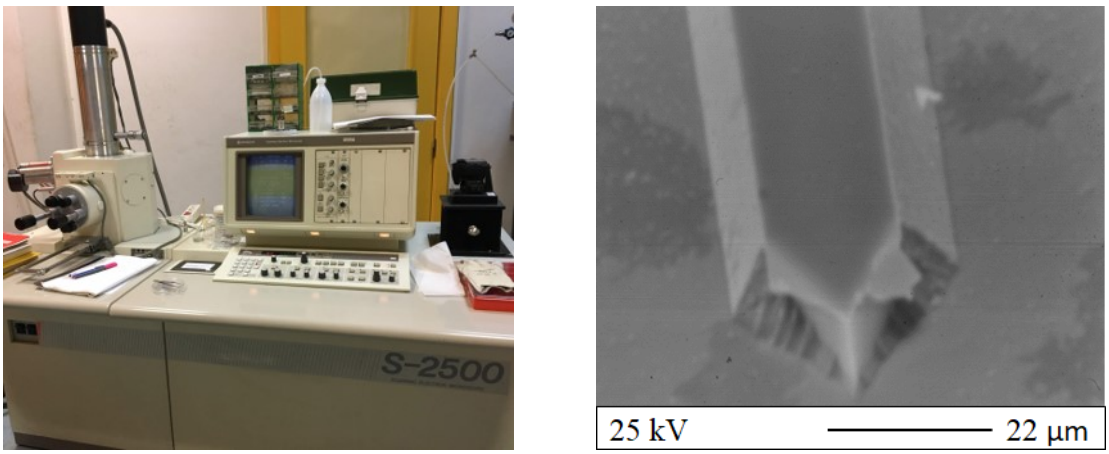

(a) (b)

Figure 3.8: (a) S-2500 Scanning Electron Microscope and (b) cantilever beam still attached to the substrate.

3.3 Cantilever Characterisation

3.3.1 Sader Method

The cantilever stiffness constant (k) can be obtained using the Sader Method [34, 35]. This method requires the plane view dimensions (L and W), which are easily obtained with an optical microscope, the resonant frequency (ω_f), and quality factor (Q_f) of the cantilever on the fluid it is being used on, which are obtained by fitting a Lorentzian function to the frequency spectrum:

$$L = \frac{a}{\left(\frac{\omega_f - \omega}{\omega_f / Q_f}\right)^2 + 1}, \tag{3.1}$$

where a is the amplitude signal at ω_f. The cantilever stiffness constant is given by:

$$k = 0.1906 \rho_f W^2 L Q_f \Gamma_i(\omega_f) \omega_f^2, \tag{3.2}$$

where ρ_f is the density of the fluid and $\Gamma_i(\omega_f)$ is the imaginary component of the hydrodynamic function Γ (Figure 3.9b).

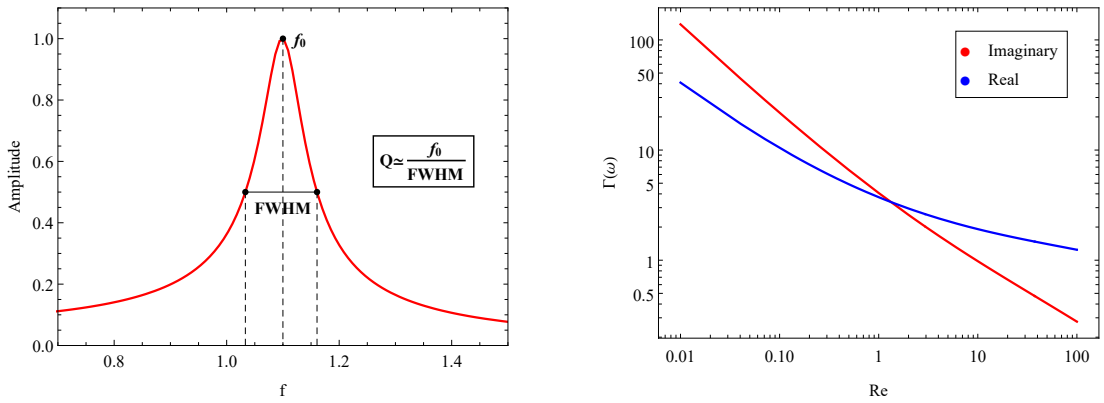

(a) (b)

Figure 3.9: (a) Fitted parameters on a frequency spectrum and (b) real and imaginary components of the hydrodynamic function $\Gamma(\omega)$ as a function of the Reynolds Number (Adopted from [35]).

Chapter 4

Results and Discussion

In this chapter, the procedure to obtain silicon and silicon nitride cantilever probes is analysed together with the practical results obtained during the fabrication. Furthermore, the possible causes and solutions for the encountered problems during the fabrication are discussed.

4.1 Silicon Probe Fabrication

The silicon cantilever fabrication process was based on bulk micromachining [8, 36–38]. The fabrication steps are represented in Figure 4.1, and the used CAD mask in Figure I.1. Starting from a 675 µm thick (100) one-side polished silicon wafer coated with Si_3N_4 on both sides, the cantilever length and width are defined on the first lithography and reactive ion etching (RIE) (Figure 4.1b). The thickness is then defined by the time the sample undergoes a KOH wet etch (Figure 4.1c). Now the defined structures need to be protected from the next KOH etch. For that, a protective layer resistant to the KOH etch is deposited on top (Figure 4.1d). Finally, the support for holding the cantilever is defined on the other side of the wafer (Figure 4.1e). The cantilever becomes a suspended structure when the final KOH etch reaches the step formed by the cantilever thickness, which was first defined in the first lithography (Figure 4.1f).

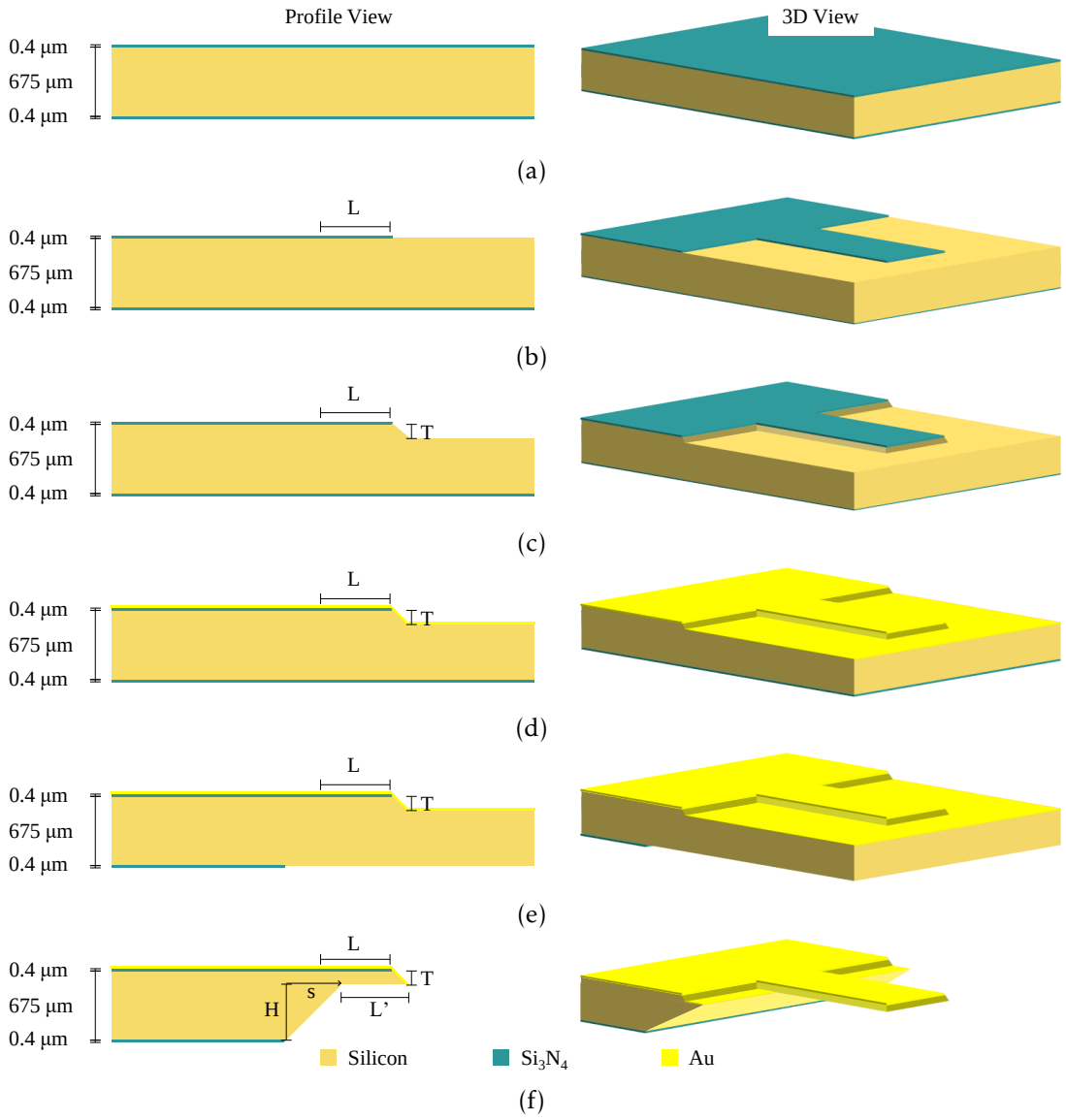

Figure 4.1: Fabrication steps for the silicon probe: (a) Silicon wafer with Si_3N_4, (b) Photolitography + RIE, (c) 28 % (m/m) KOH wet etch, (d) Metalisation, (e) Photolitography + RIE and (f) KOH wet etch.

(a) (b)

Figure 4.2: Micrographs of (a) printed cantilevers after the first lithography and RIE and (b) the same cantilevers with a thickness of 10 µm after the KOH etch.

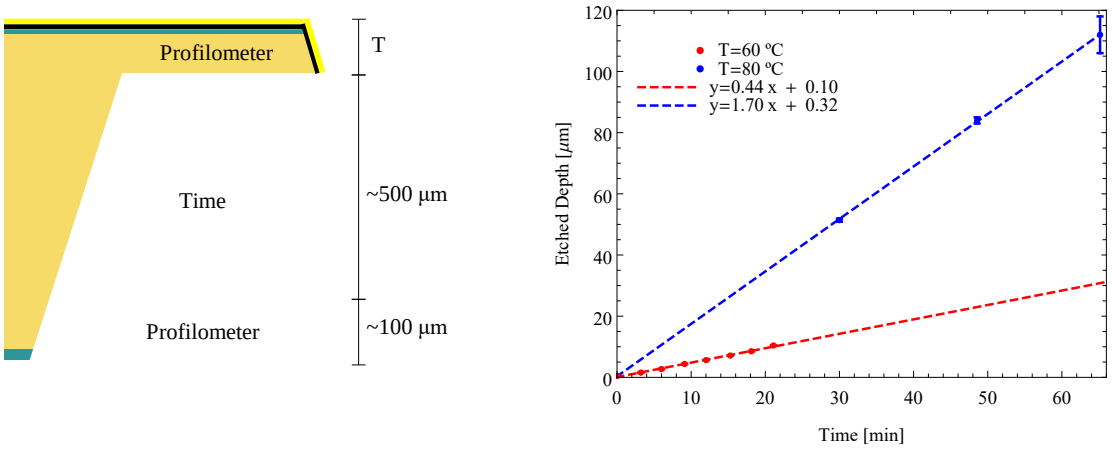

(a) (b)

Figure 4.3: (a) Cross-section representation of the wafer thickness control and (b) etch rate of the (100) plane for a temperature of 60 ºC and 80 ºC.

10 µm thick cantilever

This procedure was first tested to obtain a 10 µm thick probe. The features were well defined after the first lithography and RIE (Figure 4.2a). During the KOH etch the cantilever thickness was monitored by measuring the resulting step with a profilometer for several steps of time (Figure 4.3b). This KOH etch was performed at a temperature of 60 ºC resulting in a slow etch rate of (0.44 ± 0.01) µm/min allowing a good control of the cantilever thickness. Figure 4.2b shows the cantilevers with a thickness of 10 µm after this step, their outline is dark because the anisotropic silicon etch leaves a slope, the (111) plane, which does not reflect the light back to the microscope.

To etch greater depths, the KOH bath is maintained at a higher temperature of T=80 ºC, resulting in a etch rate of (1.70 ± 0.02) µm/min. Since the profilometer can only measure steps up to 120 µm in depth, the control of the depth after this is done through time (Figure 4.3a).

The sample containing the 10 µm thick cantilevers was divided in two. One of the

parts was further processed to additional steps to add a tip at the end of the cantilever. To add a tip onto the cantilever, after the KOH etch (Figure 4.1c), a second lithography defines a square in the cantilever (Figure 4.4a). The sample then undergoes a KOH etch in which the cantilever structure is etched further in the downward direction and silicon underneath the square is etched away (Figure 4.4b). The tip is formed when the square suffers lift-off (Figure 4.4c). The following steps are the same as for the simple beam.

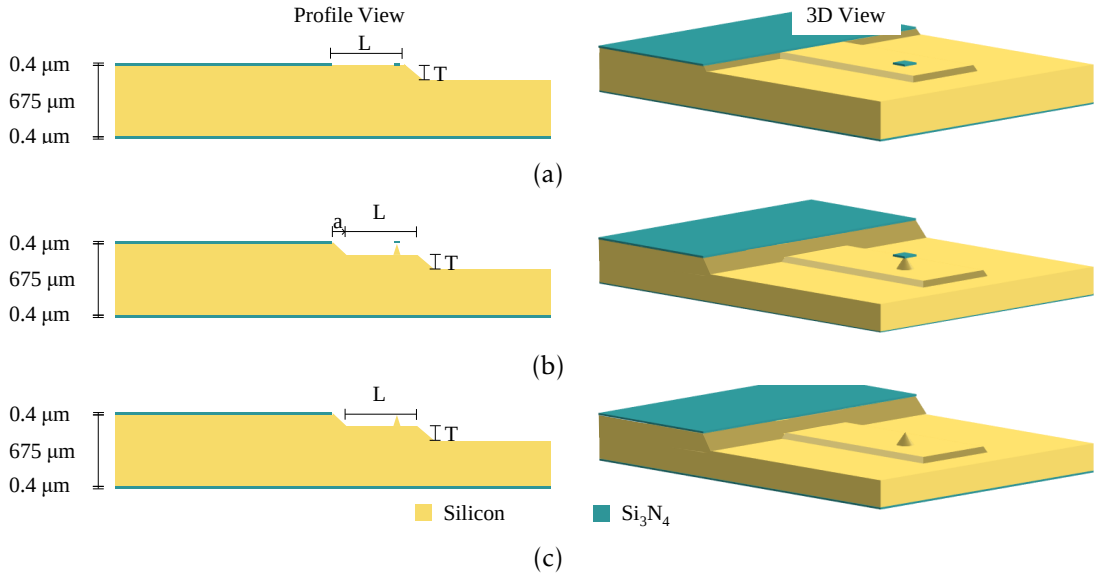

Figure 4.4: Additional fabrication steps to add a tip: (a) lithography and RIE, (b) 28 % (m/m) KOH etch and (c) square lift-off.

The second lithography that was performed did not succeed in correctly defining the square on top of the structure (Figure 4.5a). This can be due to two reasons. First, because the PR is dispensed by spin coating: for a uniform sample, the PR would spread uniformly with a thickness of 1.5 µm, but since the sample had structures with 10 µm in height, the PR probably did not spread uniformly enough and might have accumulated in some structure steps, since the these are relatively larger than the PR thickness. This then becomes a problem during the exposure to the laser, because some parts of the sample required more time/energy during the exposure. Second, also during the exposure, the laser might not focus well across all the sample due to different 10 µm steps, not defining the structures how they were supposed to be.

On the other part of the sample, containing the simple cantilevers, it was deposited 10 Å of Ti and 2000 Å of Au to understand if these metals could withstand a long KOH etch (> 3 h) and also for SEM analysis of the structures. After 1 h of KOH etch, the gold started to peel-off from the sample (Figure 4.5b). This peel-off could be due to the 10 µm thick structures not having a good step coverage, allowing the KOH to directly etch the silicon underneath it.

Due to these limitations on the lithography and on the protection of the structures, the fabrication of the 10 µm thick cantilever proved rather difficult. A 1 µm thick silicon

cantilever was tested afterwards.

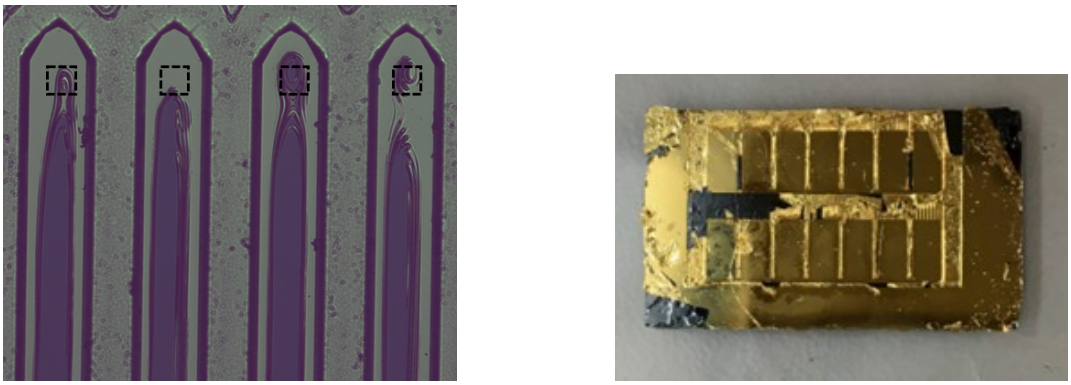

(a) (b)

Figure 4.5: (a) Micrograph of the 10 µm thick cantilevers where the squares from the second lithography are not well defined and (b) Peel-off of the gold layer after 1 h of KOH etch.

1 µm thick cantilever

The same steps were followed and the resulting structures are presented in Figure 4.6. The squares to be printed on top of the cantilever are well defined unlike the ones from the 10 µm thick cantilevers. The sample then underwent a KOH etch to define the tip, it can be seen that the sides of the cantilever become more irregular the longer the etch time, no longer becoming a uniform rectangular beam. In the SEM Micrograph (Figure 4.6e) the cantilever has a conical tip with the Si_3N_4 on top of it which has not suffered lift-off.

400 Å of Cr + Au was deposited on top of these structures for protection. On the backside of the sample, a lithography and RIE defined the chip for the cantilevers (Figure 4.7a). The lithography mask for the chip definition of the backside (red lines in Figure I.1) is dimensioned so that the silicon slope will reach the beginning of the cantilever. As shown in Figure 4.1f, the slope reaches the cantilever shifted by S from where it was originally marked in the lithography. If this lithography is misaligned with the first one, the cantilever length will change to L'.

The sample then underwent the last KOH step, however, after 1 h of this etch the Cr + Au were no longer in the sample. These metals are not reported being used in known cantilever fabrication processes, however, due to their low etch rate to KOH and due to the incapability to deposit Si_3N_4 and SiO_2 at that time of the fabrication, these metals were tested.

As the KOH etch continued, the Si_3N_4 on the backside also started to be etched away. Since it was to define the chip (macroscopic dimension), it was only necessary that the Si_3N_4 protected the chip. After 2 hours of KOH etch at 80 °C, the Si_3N_4 was all etched away leaving the chip unprotected (Figure 4.7b). This step required at least 7 hours of KOH etch, so it was necessary either a thicker Si_3N_4 layer or for the backside to be

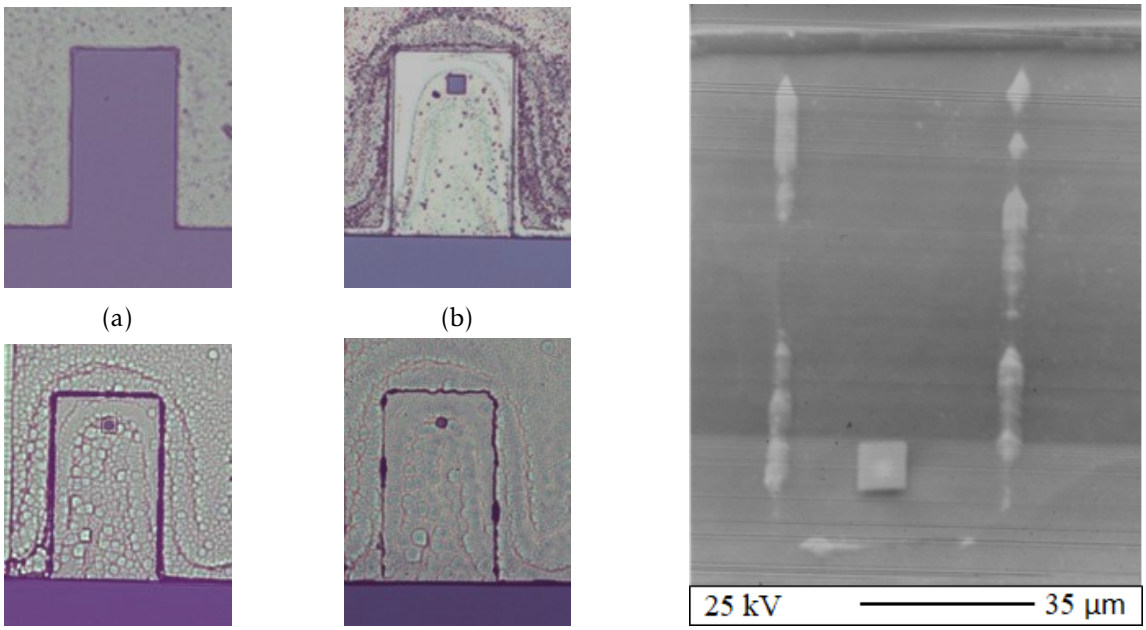

(a) (b) (c) (d) (e)

Figure 4.6: Micrographs of the cantilever after (a) the first lithography and RIE, (b) the second lithography and RIE, (c) 4 min of KOH etch and (d) 6 min of KOH. (e) SEM Micrograph of a 1 µm thick silicon cantilever with a tip on it.

(a) (b)

Figure 4.7: (a) Picture of the back side of an unpolished sample after the lithography and RIE and (b) after 1 h of KOH etch.

polished so the Si_3N_4 is not etched easily.

Since the last KOH etch would be monitored through time and the silicon wafer has a thickness of 675 µm with an uncertainty of 25 µm, this would pose a difficulty in stopping the process before the 1 µm thick cantilever was all etched away. On the other hand, this would be easier to avoid/control with a thicker cantilever but the cantilever would remain a simple beam since defining more structures revealed to be difficult. For these reasons, afterwards, a process to obtain a Si_3N_4 probe was tried, since the problem of the silicon being etched away if the process is not well monitored can be avoid if the material of the probe is not etched easily.

4.2 Tip Characterization

The conical tip was made by etching a square structure of Si_3N_4. To ensure a sharp-pointed tip, the Si_3N_4 protecting it should suffer lift-off during the KOH etch. This process was monitored along the KOH etch by focusing the microscope on the substrate plane and on the Si_3N_4 plane, Figure 4.8a and 4.8b respectively. The lift off occurs when the transparent square is no longer visible. These structures were then further analysed with SEM (Figure 4.8c and 4.8d).

The height of the tip is known from the amount of time the sample was exposed to KOH or by measuring a step with the profilometer. The diameter of the base of the tip is measured through images as shown in Figure 4.8a. These quantities can also be obtained through SEM profile pictures. The angle α_{con} the tip's surface makes with the surface of the sample when they are in contact was calculated and has a value of $\alpha_{con} = (65 \pm 15)°$.

The diagonal etch rate ($etch_{dia}$) underneath the Si_3N_4 was measured through several images as indicated by the red arrows in Figure 4.9a. This etch rate was obtained from the slope of the linear regression shown in Figure 4.9c, and it has a value of (0.76 ± 0.02) µm/min at a temperature of 60 °C.

To have a tip with a height h_{tip}, the width of the Si_3N_4 square which is going to be printed (W_{lit}) can be estimated using the previously calculated etch rate ($etch_{dia}$). Taking into account the evolution of the structure over time (Figure 4.9a), the width to be printed is:

$$W_{lit} \approx \sqrt{2} h_{tip} \frac{etch_{dia}}{etch_{100}}. \tag{4.1}$$

The inverted pyramidal tip was achieved by leaving a square of silicon unprotected by Si_3N_4. The pyramid is formed during the KOH etch as shown in Figure 4.9b. To have a tip of height h_{tip}, the width of the exposed silicon is given by the angle of the (111) plane:

$$W_{lit} = 2 h_{tip} \tan(54.74°). \tag{4.2}$$

From these structures it was also possible to measure the undercut of silicon underneath the Si_3N_4 and thus the etch rate of the (111) planes: $etch_{111} = (0.21 \pm 0.02)$ µm/min.

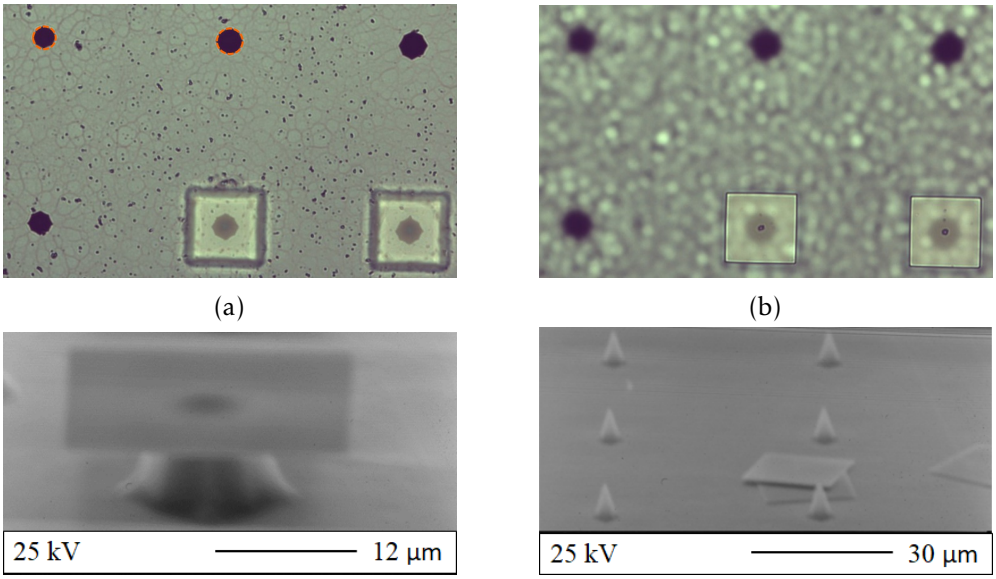

Figure 4.8: Control of the tip through micrographs by optical microscope focused on (a) the substrate plane and (b) Si_3N_4 plane. (c) SEM micrograph of a tip with the Si_3N_4 square on top of it and (d) tips after lift-off.

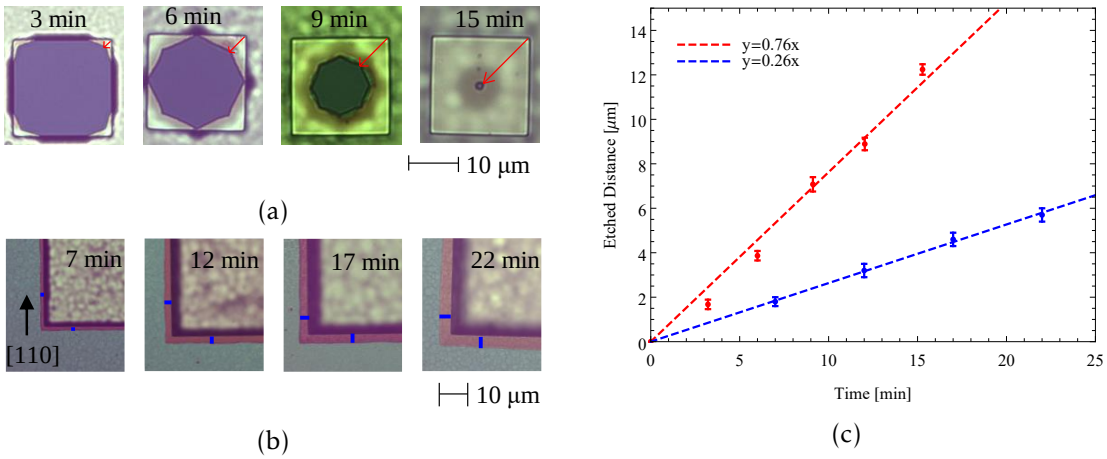

Figure 4.9: (a) Method used to measure the etch rate beneath the Si_3N_4 for the conical tip, (b) measurement of the undercut and (c) respective etch rates for a temperature of 60 ºC.

Pyramidal tips usually have heights up to 15 µm, the undercut can be neglected when dimensioning the tip.

4.3 Silicon Nitride Probe Fabrication

The fabrication process for the Si_3N_4 probe is very similar to the one for the silicon probe and is represented in Figure 4.10. Starting with a 450 µm thick double-side polished silicon (100) wafer coated with 100 nm SiO_2 on both sides, it was deposited Si_3N_4 on both sides through plasma enhanced chemical vapour deposition (PECVD). A starting lithography and RIE are performed on one side (Figure 4.10b), defining the cantilever measurements. As explained in 3.1.1 this leaves alignment marks near the corners of the sample. These structures are now protected with a layer of Si_3N_4 deposited by PECVD (Figure 4.10c). On the other side of the sample, a second lithography and RIE define the chips to handle the cantilevers (Figure 4.10d). The sample then undergoes a KOH etch, etching more than half of the wafer thickness (Figure 4.10e). Since this is a long etch, the corners of the sample also get etched, and this is the reason why the first lithography was done: to leave alignment marks. A third lithography and RIE are performed on the first side defining the cantilevers again (Figure 4.10f). The cantilevers become a suspended structure when, during the KOH etch, the exposed silicon is all etched away (Figure 4.10g).

The first lithography was successful in defining the cantilever's width and length, then through the PECVD step, a layer of 0.5 µm of SiO_2 plus 1 µm of Si_3N_4 was deposited to protect this side of the sample from etching with the KOH bath. The alignment marks remain visible after this step (Figure 4.11a). On the other side of the sample, a lithography and RIE define the chip outline, as it was done for the silicon probe.

After 1 h of the KOH etch, the Si_3N_4 on both sides started to peel-off (Figure 4.11). This may be due to both sides of the sample touching several surfaces during some processes, which may result in scratches and contamination, allowing the KOH to directly attack the silicon. Another cause may be the adhesion of the Si_3N_4 to the silicon, in Figure 4.11c the first deposited Si_3N_4, remains during the KOH etch, however the one that was deposited to protect the structures suffered peel-off. Between the lithography and the CVD the silicon may gain layers of SiO_2, adhered water or contamination that can make the adhesion less strong.

From the established procedures from where the process was based, the protecting layer of SiO_2 and Si_3N_4 can either be produced by thermal oxidation and Low Pressure CVD having thickness of 100 nm and 120 nm for a 350 µm thick wafer [38], or by PECVD having thickness of 3 µm and 1 µm for a 300 µm thick wafer [36]. In the tested process it was only possible to deposit 0.5 µm and 1 µm of SiO_2 and Si_3N_4. Thicker layers would resist longer KOH etch times and thinner wafers would decrease the etch time, which would ease this step.

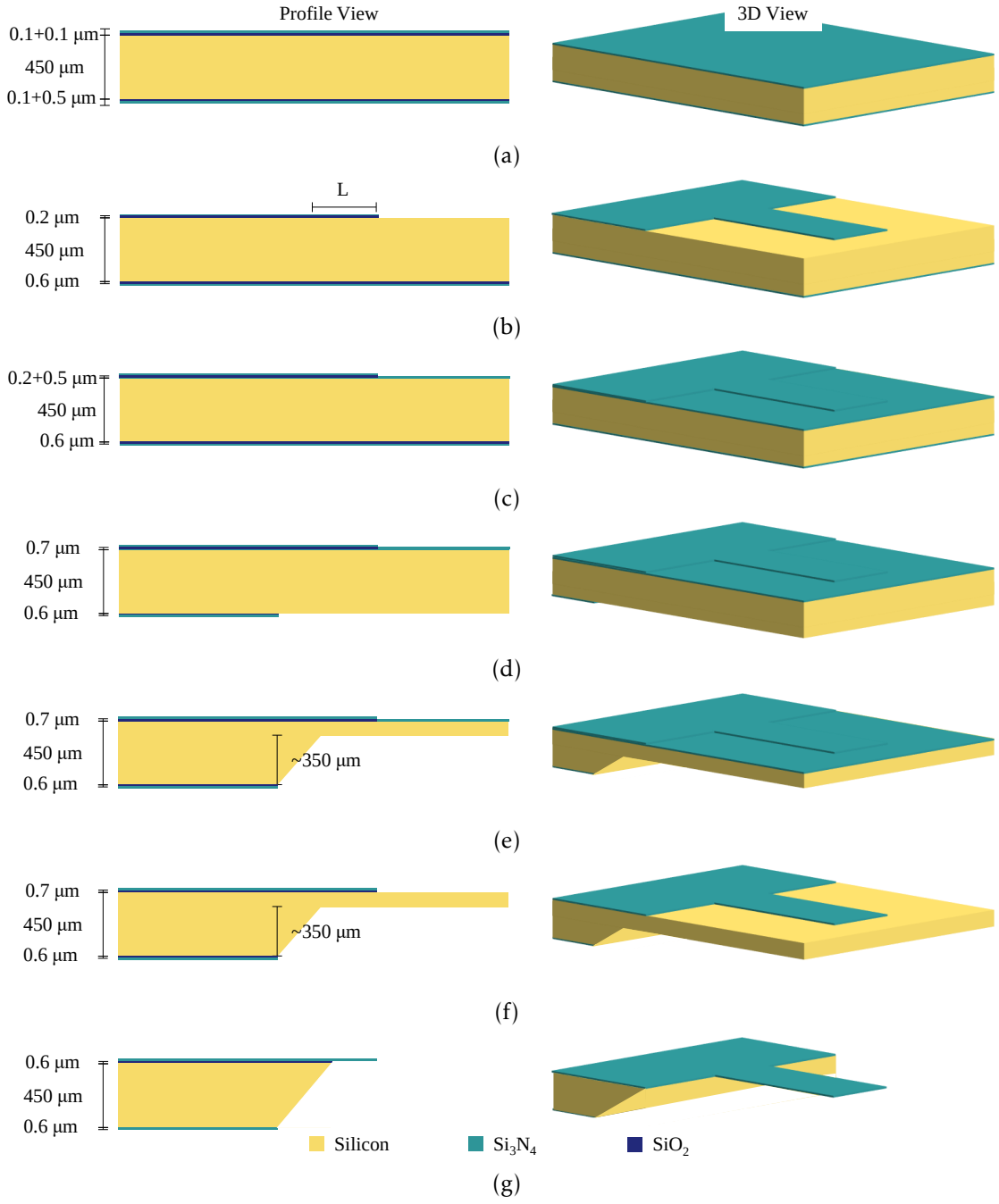

Figure 4.10: Fabrication steps for the silicon nitride probe: (a) Silicon wafer with Si_3N_4, (b) Photolitography + RIE, (c) CVD, (d) Photolitography + RIE on the other side, (e) 28 % (m/m) KOH wet etch, (f) Photolitography + RIE and (g) KOH wet etch.

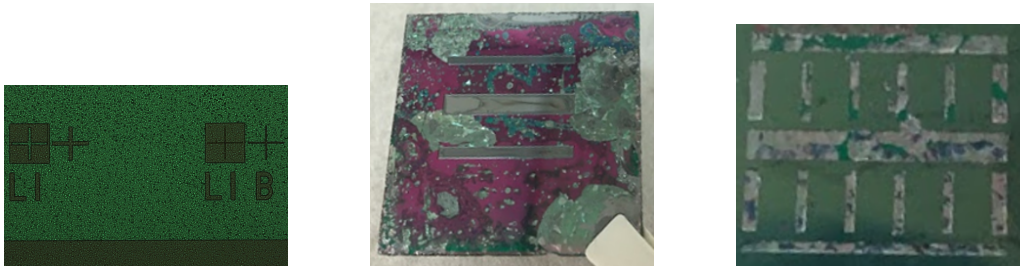

(a) (b) (c)

Figure 4.11: (a) Micrograph of the alignment marks after the PECVD and (b) picture of the back side and (b) of the front side of the polished sample where the Si_3N_4 protecting the structures peeled off after 1 h of KOH etch.

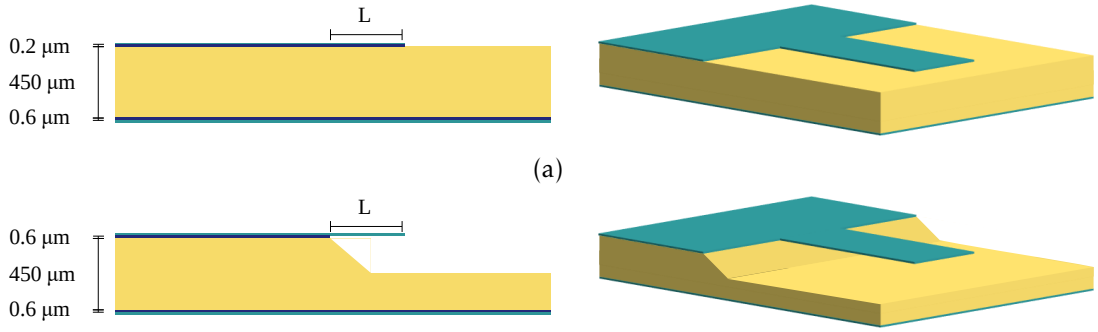

Figure 4.12: Fabrication steps for the silicon nitride probe: (a) Lithography + RIE and (b) 28 % (m/m) KOH etch.

To enable the characterisation of the cantilevers and its materials, a set was produced by a simpler method as described in Figure 4.12. The amount of Si_3N_4 deposited by PECVD defines the thickness of the cantilever, and the lithography defines the other measurements. After this, the sample underwent a KOH etch. The cantilevers become suspended as the silicon underneath the Si_3N_4 starts to etch (Figure 4.13a and 4.13b). As the etch continues these structures become totally suspended as shown in Figure 4.13c and 4.13d and schematized in Figure 4.12b. The longer cantilevers may sometimes break due to the capillary forces between the cantilever and the surface below it (Figure 4.14a and 4.14b). To allow the visualisation of these through SEM and to have a reflective layer on top of the cantilever, a layer of 400 Å of Cr + Au was deposited through magnetron sputtering. After this, the structures were still standing and presented some curvature as can be seen in the SEM micrograph and through the incapability to keep the whole cantilever in the focal plane of the microscope (Figure 4.13e and 4.13f). Although these cantilevers were successfully fabricated, they are not suitable for AFM due to the slope of the silicon in the chip that shadows the cantilever (Figure 4.15b), however it is useful for analysing their mechanical properties (f, Q and k).

The long KOH etch, from the original method (Figure 4.10e), is done on the chip side

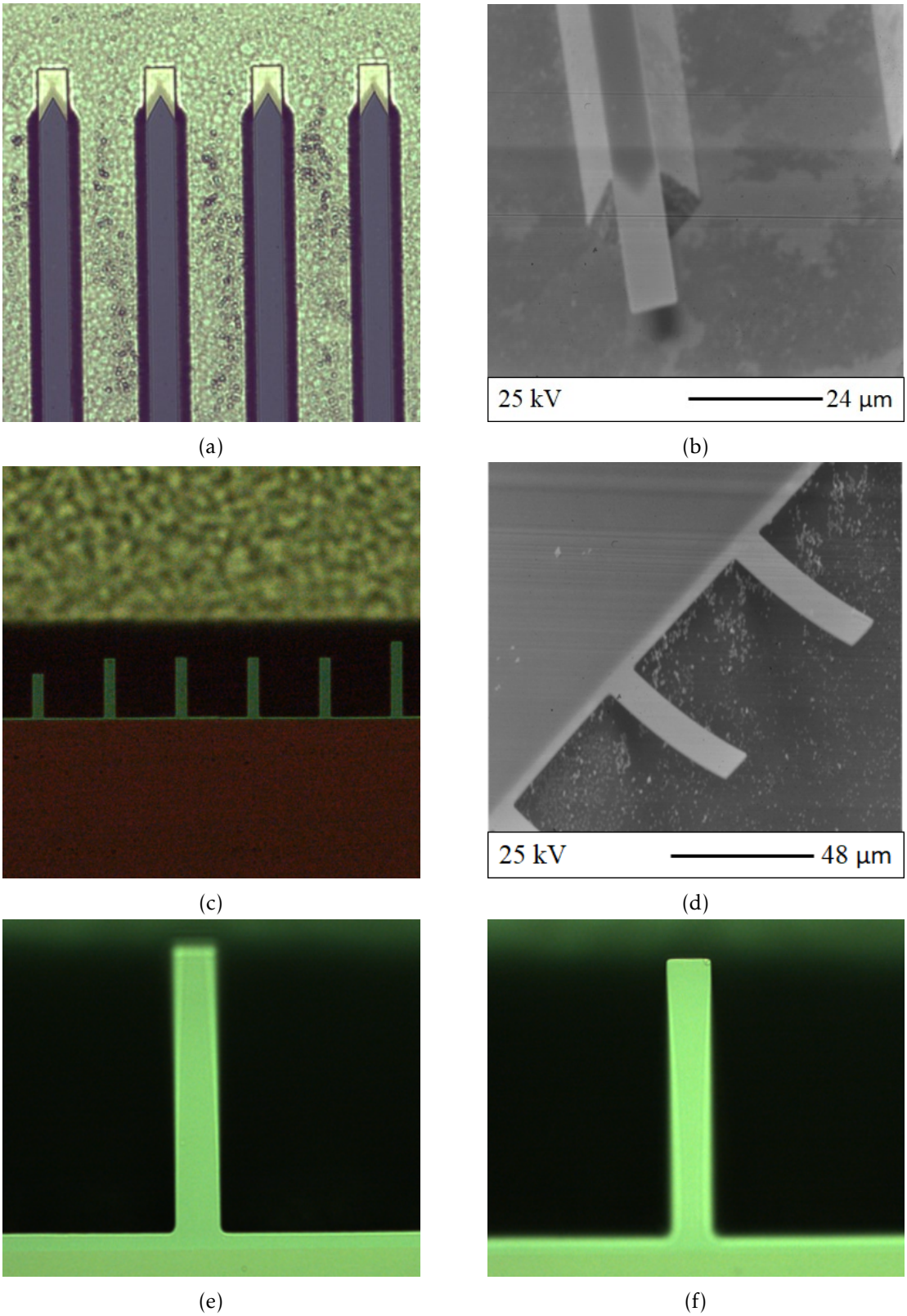

(a) (b) (c) (d) (e) (f)

Figure 4.13: Process evolution of the cantilevers becoming suspended structures: (a) Micrograpgh of the cantilever with silicon underneath it without the gold coating and (b) SEM micrograph of the same cantilevers with gold coating. Suspended cantilevers (c) before and (d) after the gold coating. Coated cantilever focused on its base and (f) focused on its end.

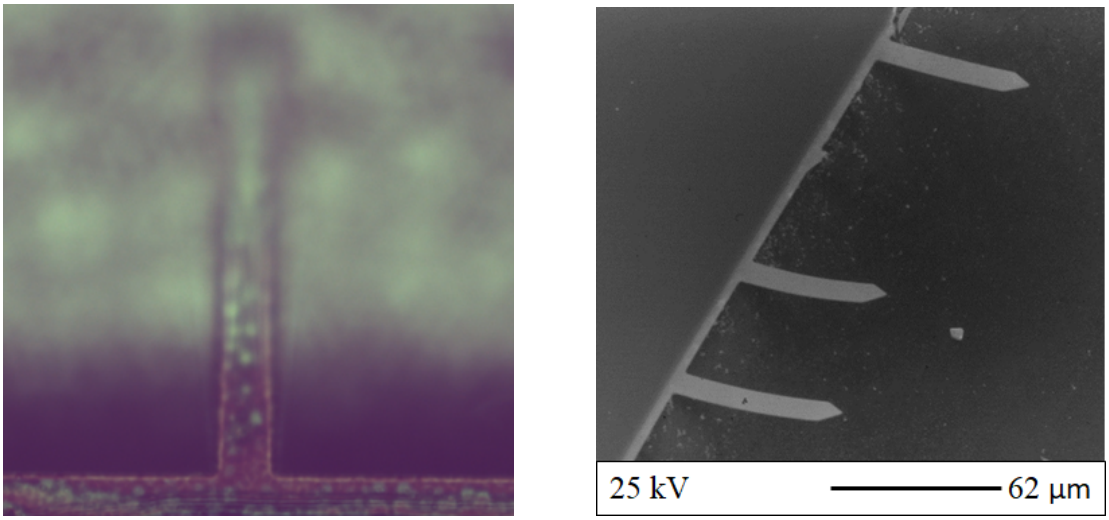

(a) (b)

Figure 4.14: (a) Bending of the cantilever due to capillary forces and (b) missing cantilever.

so that the cantilevers can be used for AFM (Figure 4.15a). As explained in Section 2.2 a laser is pointed at the end of the cantilever which is reflected back to a photosensor. Due to the anisotropic silicon etch, if the etch is done on the cantilever side, the silicon slope will block the reflection of the laser (Figure 4.15b), and while flipping the chip unblocks it, the sample no longer fits underneath.

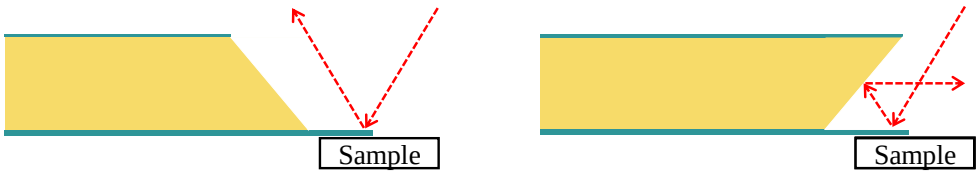

(a) (b)

Figure 4.15: (a) Chip that allows the cantilever use for AFM and (b) that does not allow.

4.4 Channel Definition

The approach to make a hollow channel inside the cantilever was based on a sacrificial layer [39–41]. A layer of 1 µm Si_3N_4 followed by another of 0.5 µm SiO_2 is deposited by PECVD (Figure 4.16a). A lithography then defines the channel measurements and the layer of SiO_2 is etched by RIE (Figure 4.16b). During the RIE step it was clear that the etch was not uniform (Figure 4.17a) across the sample. The sample was over-etched to ensure that all the SiO_2 was removed, so that the channel could be formed afterwards. After this, the channel presented a height of (0.7 ± 0.2) µm. Afterwards, 0.6 µm of Si_3N_4 was deposited by PECVD to seal the channel, since the method presents good conformity the Si_3N_4 will be deposited vertically and horizontally on the SiO_2 surfaces (Figure 4.16c).

To verify if the etch of SiO_2 was controllable during the KOH etch, the sample was broken transversely to the channel's orientation, allowing the KOH to etch the SiO_2. After 1 h of KOH etch, the channel height was measured and remained the same, however it was not possible to observe through the microscope (Figure 4.17b) if the SiO_2 was being etched (as it was during the tip process). The monitorisation of the SiO_2 etch is then controlled by time. From a calibration sample, the etch rate of the SiO_2 in KOH at 80 ºC was measured as 30 nm/min, which can be considered slow since the cantilevers can be relatively long. Either SiO_2 is replaced by Si to form the channel, or instead of etching with KOH it can be etched by hydrofluoric acid (HF) which presents a higher etch rate but is more hazardous.

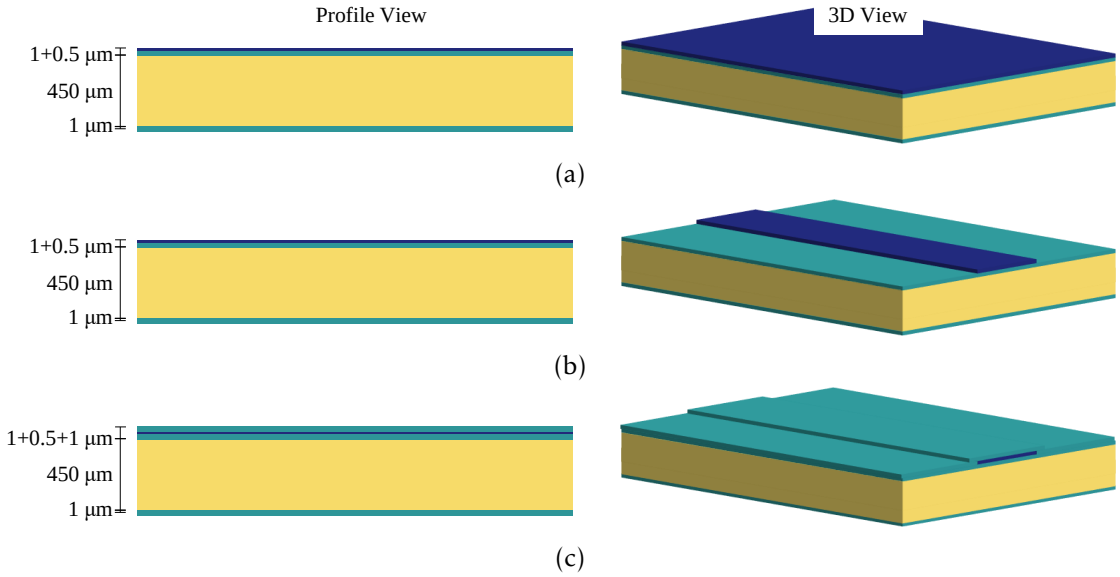

Figure 4.16: Fabrication steps for the hollow silicon nitride channel: (a) CVD, (b) Photolithography + RIE, (c) CVD and (d) 28 % (m/m) KOH wet etch.

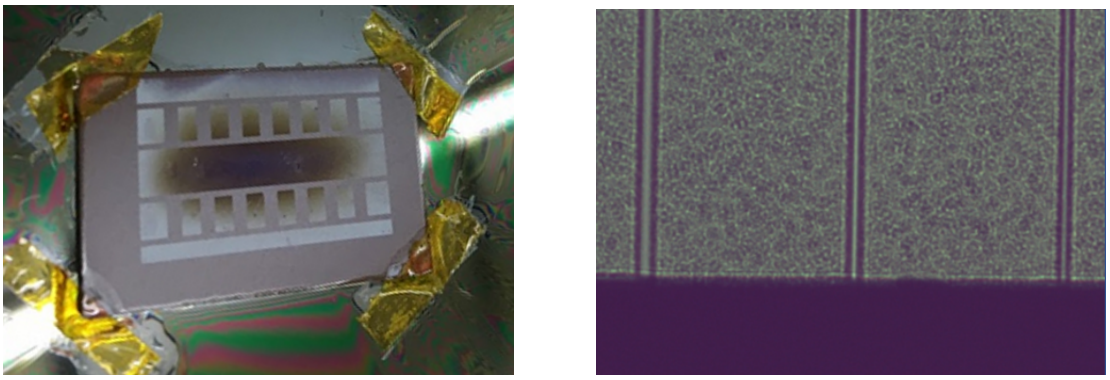

(a) (b)

Figure 4.17: (a) Picture of the non-uniform RIE of the channels and (b) micrograph of the channels on the cleavage side, the channels' width are 2, 4 and 6 µm.

Chapter 5

Conclusions

This work presents a microfabrication procedure to obtain a cantilever through microbulking. The viability of each step of the process, together with the quantification of some parameters and the choice of materials were studied.

Initially it was tested a procedure to obtain a silicon probe with and without a tip. In this stage it was measured the silicon (100) plane etch rate for a KOH solution of 85% (m/m), which resulted in (0.44 ± 0.01) µm/min and (1.70 ± 0.01) µm/min for a temperature of 60 ºC and 80 ºC respectively.

It was possible to obtain a simple cantilever beam, attached to the substrate, with a thickness of 10 µm. This cantilever did not withstand the longer KOH etch due to the materials used (titanium and gold) for the protective layer. The lithography step to define the tip on top of a 10 µm thick beam did not lead to a well-defined structure. This could be due to the laser not focusing on the 10 µm separate planes or due to the photoresist not having a good uniformity across the sample. Since it was not possible to obtain a tip on a beam of this thickness, a 1 µm thick silicon cantilever was tested. The lithography step successfully defined a tip on a beam of this thickness, however, the beam's outline became irregular in the process. These beams were protected with a chromium and gold layer that also did not withstand the longer KOH etch. Aside from that, the control and monitorisation of the last KOH etch would reveal to be difficult since these beams would rapidly etch away. These silicon beams were fabricated from a wafer with a polished and an unpolished side. The chip was defined on the unpolished side since it was of macroscopic dimensions, where the outline was not required to have a high resolution. However, the Si_3N_4 that defined the structure was etched after 2 hours of KOH etch, leaving the chip unprotected. Because of this, new double-sided polished wafers were used for the fabrication of Si_3N_4 probes.

The tips were successfully fabricated and characterised together with their fabrication parameters, regardless of the fabrication of the beams. Two tips were obtained: a conical and a pyramidal tip. The tips form from an anisotropic etch underneath the printed Si_3N_4 square, this etch was measured and has a value $etch_{dia} = (0.76 \pm 0.02)$ µm/min when forming a conical tip with an angle of $\alpha_{con} = (65 \pm 15)°$, and it was measured an

undercut etch rate of $etch_{111} = (0.21 \pm 0.02)$ µm/min for the (111) planes when forming the inverted pyramidal tip.

The procedure to obtain Si_3N_4 probes was very similar to silicon probes and it avoids the problem of the probe being overetched, since the material resists KOH. Here it was possible to deposit SiO_2 and Si_3N_4 (0.6 µm) to protect the structures, however, after 2 hours of etch time these layers would be etched away. It was possible to obtain suspended cantilevers, however, due to the chip format these could not be used in atomic force microscopy since they do not simultaneously allow sample interaction and the laser on top of the cantilever. Based on this, future work should focus on trying different thicknesses of Si_3N_4 so the sample can sustain KOH etches longer than 3 h, and with this obtain cantilevers in a chip which allows interaction with the sample.

Regarding the channels, it was possible to observe that they did not collapse after the sacrificial layer was removed from underneath them.

With FEM, it was possible to observe different behaviour regarding the geometric parameters which are not described by the analytical model. This allows the analysis of more complex geometries, which would otherwise require the development of different analytical models. However, the accuracy of the results could not be verified due to the impossibility to obtain experimental data. The chips containing the cantilevers for characterisation were larger than the AFM support, so they were attached to the stage which could not reach amplitudes that would make the cantilevers oscillate. Due to the COVID-19 pandemic, it was not possible to test other solutions for the cantilevers characterisation. With this characterisation, it would have been possible to deduce $\sqrt{E/\rho}$ for the deposited Si_3N_4, so that future cantilevers can be better dimensioned. The cantilevers with an arrow end and with parallel beams should be characterized to understand if the Δf is of the same magnitude as expected from Comsol.

Bibliography

[1] R. R. Grüter, J. Vörös, and T. Zambelli. "FluidFM as a lithography tool in liquid: spatially controlled deposition of fluorescent nanoparticles." In: *Nanoscale* 5.3 (2013), pp. 1097–1104. DOI: 10.1039/C2NR33214K.

[2] L. Fabié, P. Agostini, M. Stopel, C. Blum, B. Lassagne, V. Subramaniam, and T. Ondarçuhu. "Direct patterning of nanoparticles and biomolecules by liquid nanodispensing." In: *Nanoscale* 7.10 (2015), pp. 4497–4504. DOI: 10.1039/c4nr06824f.

[3] R. van Oorschot, H. H. Perez Garza, R. J. S. Derks, U. Staufer, and M. K. Ghatkesar. "A microfluidic AFM cantilever based dispensing and aspiration platform." In: *EPJ Techniques and Instrumentation* 2.1 (2015), p. 4. DOI: 10.1140/epjti/s40485-014-0012-4.

[4] F. Heuck, T. Hug, T. Akiyama, P. Frederix, A. Engel, A. Meister, H. Heinzelmann, N. de Rooij, and U. Staufer. "Evaporation based micro pump integrated into a scanning force microscope probe." In: *Microelectronic Engineering* 85.5-6 (2008), pp. 1302–1305. DOI: 10.1016/J.MEE.2007.12.047.

[5] H. H. Perez Garza, M. K. Ghatkesar, and U. Staufer. "Aspiration through hollow cantilever-based nanopipette by means of evaporation." In: *Micro & Nano Letters* 8.11 (2013), pp. 758–761. DOI: 10.1049/mnl.2013.0362.

[6] M. K. Ghatkesar, H. H. P. Garza, and U. Staufer. "Hollow AFM cantilever pipette." In: *Microelectronic Engineering* 124 (2014), pp. 22–25. DOI: 10.1016/J.MEE.2014.04.019.

[7] R. D. Piner, J. Zhu, F. Xu, S. Hong, and C. A. Mirkin. ""Dip-Pen"Nanolithography." In: *Science* 283.5402 (1999), pp. 661–663. DOI: 10.1126/science.283.5402.661.

[8] A. Meister, S. Jeney, M. Liley, T. Akiyama, U. Staufer, N. de Rooij, and H. Heinzelmann. "Nanoscale dispensing of liquids through cantilevered probes." In: *Microelectronic Engineering* 67-68 (2003), pp. 644–650. DOI: 10.1016/S0167-9317(03)00126-6.

[9] K. H. Kim, N. Moldovan, C. Ke, and H. D. Espinosa. "A novel AFM chip for fountain pen nanolithography - Design and microfabrication." In: *Materials Research Society Symposium - Proceedings*. Vol. 782. 2003, pp. 267–272. DOI: 10.1557/proc-782-a5.56.

[10] T. Hug, T. Biss, N. de Rooij, and U. Staufer. "Generic fabriction technology for transparent and suspended microfluidic and nanofluidic channels." In: *The 13th International Conference on Solid-State Sensors, Actuators and Microsystems, 2005. Digest of Technical Papers. TRANSDUCERS '05.* Vol. 2. IEEE, pp. 1191–1194. DOI: 10.1109/SENSOR.2005.1497291.

[11] F. Heuck. "Developing and Analysing sub-10 µm Fluidic Systems with Integrated Electrodes for Pumping and Sensing in Nanotechnology Applications." Doctoral dissertation. Mechanical, Maritime and Materials Engineering, 2010.

[12] M. Ghatkesar, H. Garza, F. Heuck, and U. Staufer. "Scanning Probe Microscope-Based Fluid Dispensing." In: *Micromachines* 5.4 (2014), pp. 954–1001. DOI: 10.3390/mi5040954.

[13] A. Meister, J. Przybylska, P. Niedermann, C. Santschi, and H. Heinzelmann. "Hollow Atomic Force Microscopy Probes for Nanoscale Dispensing of Liquids." In: *NSTI Nanotech* 3 (2008), pp. 273–276.

[14] T. Zambelli, M. J. Aebersold, P. Behr, H. Han, L. Hirt, V. Martinez, O. Guillaume-Gentil, and J. Vörös. "FluidFM: Development of the Instrument as well as Its Applications for 2D and 3D Lithography." In: *Open-Space Microfluidics: Concepts, Implementations, Applications*. Weinheim, Germany: Wiley-VCH Verlag GmbH & Co. KGaA, 2018, pp. 295–323. DOI: 10.1002/9783527696789.ch14.

[15] M. K. Ghatkesar, H. H. P. Garza, and U. Staufer. "Hollow AFM cantilever pipette." In: *Microelectronic Engineering* 124 (2014), pp. 22–25. DOI: 10.1016/j.mee.2014.04.019.

[16] E. J. W. Berenschot, N. Burouni, B. Schurink, J. W. van Honschoten, R. G. P. Sanders, R. Truckenmuller, H. V. Jansen, M. C. Elwenspoek, A. A. van Apeldoorn, and N. R. Tas. "3D Nanofabrication of Fluidic Components by Corner Lithography." In: *Small* 8.24 (2012), pp. 3823–3831. DOI: 10.1002/smll.201201446.

[17] N. Burouni, E. Berenschot, M. Elwenspoek, E. Sarajlic, P. Leussink, H. Jansen, and N. Tas. "Wafer-scale fabrication of nanoapertures using corner lithography." In: *Nanotechnology* 24.28 (2013), p. 285303. DOI: 10.1088/0957-4484/24/28/285303.

[18] S. Deladi, N. R. Tas, J. W. Berenschot, G. J. M. Krijnen, M. J. de Boer, J. H. de Boer, M. Peter, and M. C. Elwenspoek. "Micromachined fountain pen for atomic force microscope-based nanopatterning." In: *Applied Physics Letters* 85.22 (2004), pp. 5361–5363. DOI: 10.1063/1.1823040.

[19] N. Moldovan, K.-H. Kim, and H. Espinosa. "Design and Fabrication of a Novel Microfluidic Nanoprobe." In: *Journal of Microelectromechanical Systems* 15.1 (2006), pp. 204–213. DOI: 10.1109/JMEMS.2005.863701.

[20] G. Binnig, H. Rohrer, C. Gerber, and E. Weibel. "Surface Studies by Scanning Tunneling Microscopy." In: *Physical Review Letters* 49.1 (1982), pp. 57–61. DOI: 10.1103/PhysRevLett.49.57.

[21] G. Binnig, C. F. Quate, and C. Gerber. "Atomic Force Microscope." In: *Physical Review Letters* 56.9 (1986), pp. 930–933. DOI: 10.1103/PhysRevLett.56.930.

[22] B. Bhushan and O. Marti. "Scanning Probe Microscopy – Principle of Operation, Instrumentation, and Probes." In: *Springer Handbook of Nanotechnology*. Berlin, Heidelberg: Springer Berlin Heidelberg, 2010, pp. 573–617. DOI: 10.1007/978-3-642-02525-9_21.

[23] W. T. Thomson and M. D. Dahleh. *Theory of vibrations with applications*. Pearson, 2014, p. 524.

[24] C. Marutschke. "Three-dimensional imaging of the solid-liquid interface with high-resolution atomic force microscopy." Doctoral dissertation. 2015.

[25] R. J. R. J. Roark, W. C. W. C. Young, R. G. R. G. Budynas, and A. M. Sadegh. *Roark's formulas for stress and strain*. McGraw-Hill, 2012, p. 1054.

[26] C. A. Clifford and M. P. Seah. "The determination of atomic force microscope cantilever spring constants via dimensional methods for nanomechanical analysis." In: *Nanotechnology* 16.9 (2005), pp. 1666–1680. DOI: 10.1088/0957-4484/16/9/044.

[27] R. J. Cannara, M. Eglin, and R. W. Carpick. "Lateral force calibration in atomic force microscopy: A new lateral force calibration method and general guidelines for optimization." In: *Review of Scientific Instruments* 77.5 (2006), p. 053701. DOI: 10.1063/1.2198768.

[28] S. Schmid, L. G. Villanueva, and M. L. Roukes. "Resonance Frequency." In: *Fundamentals of Nanomechanical Resonators*. Cham: Springer International Publishing, 2016, pp. 1–56. DOI: 10.1007/978-3-319-28691-4_1.

[29] T. R. Albrecht, S. Akamine, T. E. Carver, and C. F. Quate. "Microfabrication of cantilever styli for the atomic force microscope." In: *Journal of Vacuum Science & Technology A: Vacuum, Surfaces, and Films* 8.4 (1990), pp. 3386–3396. DOI: 10.1116/1.576520.

[30] B. Lautrup. *Physics of continuous matter : exotic and everyday phenomena in the macroscopic world*. Taylor & Francis, 2011, p. 684.

[31] P. Tabeling. *Introduction to microfluidics*. Oxford University Press, 2005, p. 301.

[32] H. H. P. Garza, M. K. Ghatkesar, and U. Staufer. "Combined AFM — Nanopipette cartridge system for actively dispensing femtolitre droplets." In: *2012 International Conference on Manipulation, Manufacturing and Measurement on the Nanoscale (3M-NANO)*. IEEE, 2012, pp. 320–325. DOI: 10.1109/3M-NANO.2012.6472930.

[33] K. Williams, K. Gupta, and M. Wasilik. "Etch rates for micromachining processing-part II." In: *Journal of Microelectromechanical Systems* 12.6 (2003), pp. 761–778. DOI: 10.1109/JMEMS.2003.820936.

[34] J. E. Sader. "Frequency response of cantilever beams immersed in viscous fluids with applications to the atomic force microscope." In: *Journal of Applied Physics* 84.1 (1998), pp. 64–76. DOI: 10.1063/1.368002.

[35] J. E. Sader, J. W. M. Chon, and P. Mulvaney. "Calibration of rectangular atomic force microscope cantilevers." In: *Review of Scientific Instruments* 70.10 (1999), pp. 3967–3969. DOI: 10.1063/1.1150021.

[36] J.-d. Li, J. Xie, W. Xue, and D.-m. Wu. "Fabrication of cantilever with self-sharpening nano-silicon-tip for AFM applications." In: *Microsystem Technologies* 19.2 (2013), pp. 285–290. DOI: 10.1007/s00542-012-1622-x.

[37] B. Tang, K. Sato, H. Tanaka, and M. A. Gosalvez. "Fabrication of sharp tips with high aspect ratio by surfactant-modified wet etching for the AFM probe." In: *2011 IEEE 24th International Conference on Micro Electro Mechanical Systems*. IEEE, 2011, pp. 328–331. DOI: 10.1109/MEMSYS.2011.5734428.

[38] A. Boisen, O. Hansen, and S. Bouwstra. "AFM probes with directly fabricated tips." In: *Journal of Micromechanics and Microengineering* 6.1 (1996), pp. 58–62. DOI: 10.1088/0960-1317/6/1/012.

[39] N. Moldovan, K.-H. Kim, and H. Espinosa. "Design and Fabrication of a Novel Microfluidic Nanoprobe." In: *Journal of Microelectromechanical Systems* 15.1 (2006), pp. 204–213. DOI: 10.1109/JMEMS.2005.863701.

[40] M. Khan, S. Schmid, Z. Davis, S. Dohn, and A. Boisen. "Fabrication of resonant micro cantilevers with integrated transparent fluidic channel." In: *Microelectronic Engineering* 88.8 (2011), pp. 2300–2303. DOI: 10.1016/J.MEE.2011.02.096.

[41] A. De Pastina, D. Maillard, and L. Villanueva. "Fabrication of suspended microchannel resonators with integrated piezoelectric transduction." In: *Microelectronic Engineering* 192 (2018), pp. 83–87. DOI: 10.1016/J.MEE.2018.02.011.

Annex I

Lithography Masks

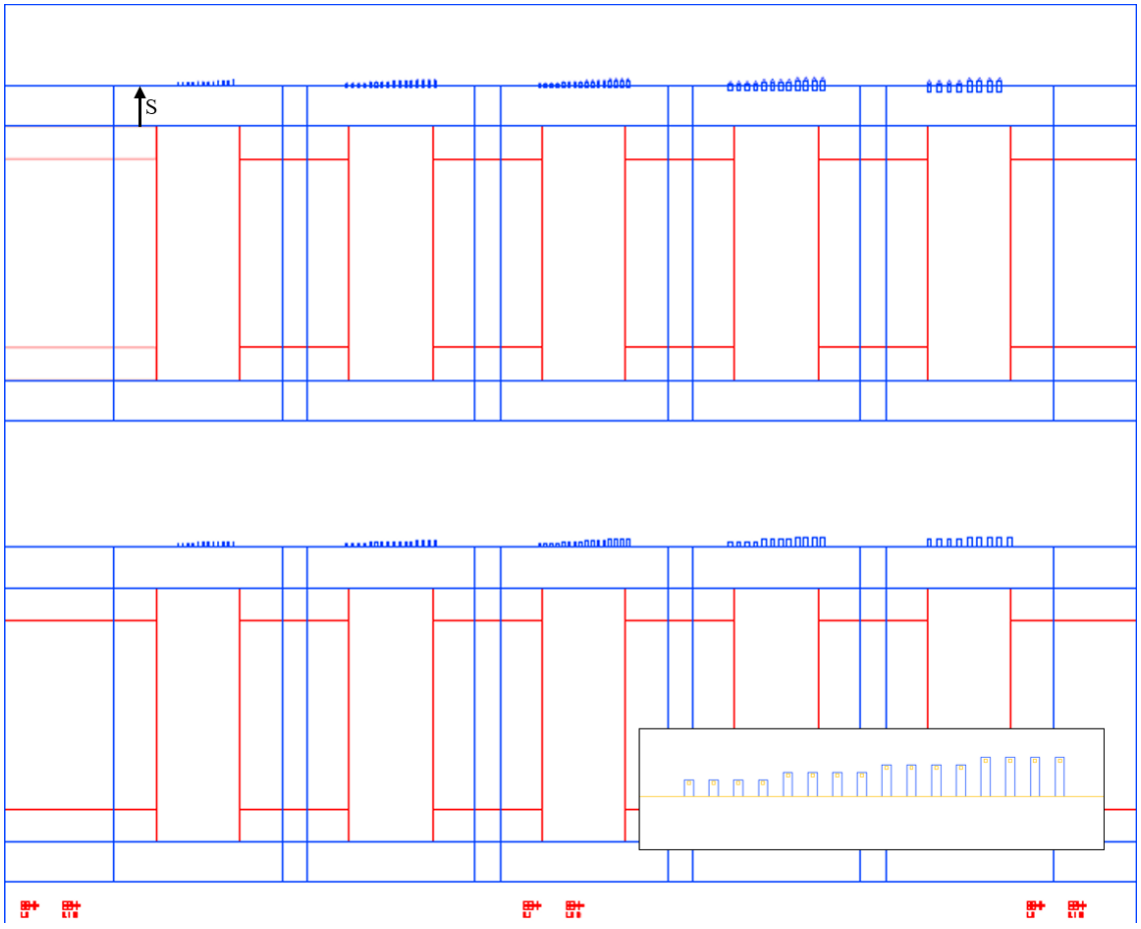

Figure I.1: CAD mask for a cantilever with tip. The yellow layer (close-up) defines the squares to form the tip, the blue layer defines the cantilever and the red layer defines the chip on the backside of the substrate.

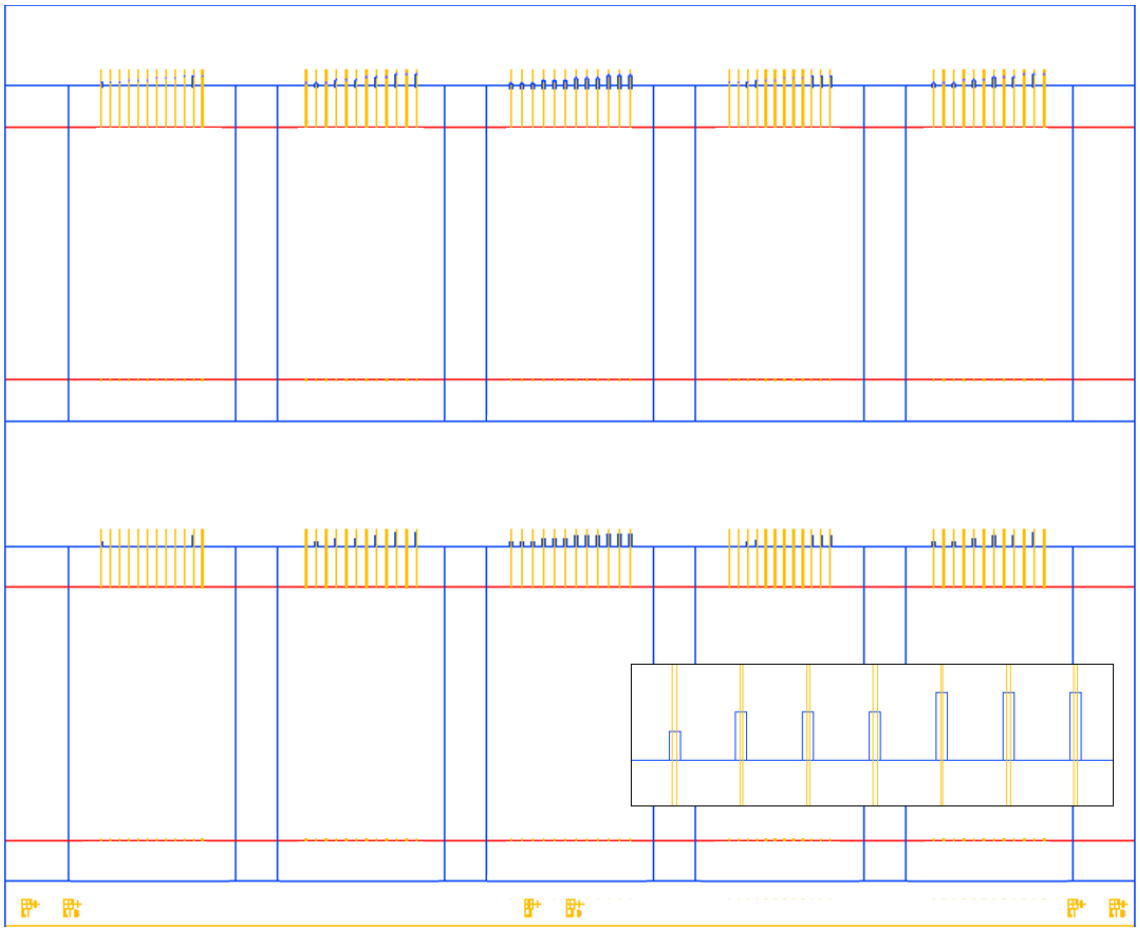

Figure I.2: CAD mask for a cantilever with a hollow section. The yellow layer (close-up) defines the hollow channel, the blue layer defines the cantilever and the red layer defines the chip on the backside of the substrate.